

Bay Area Environmental Research Institute
3430 Noriega
San Francisco, CA

FINAL TECHNICAL REPORT

Time period: September 1, 1997 through June 30, 2001

Project: NASA Cooperative Agreement No. NCC2-1000 entitled
"An Aerosol Physical Chemistry Model for the Upper
Troposphere"

Principal Investigator: Dr. Jin-Sheng Lin

Date: April 27, 2001

TABLE OF CONTENTS

I. Introduction	Pg 1
II. Tasks and Accomplishments	1
III. Publications, Presentations and Reports	2
Attachment A. Copies of Publications	

I Introduction

This report is the final report for the Cooperative Agreement NCC-2-1000. The tasks outlined in the various proposals are listed below with a brief comment as to the research performed. The publications are attached.

II. NCC 2 1000 Tasks and Accomplishments

1. Development of an aerosol chemistry model (Tasks 1-5, Dr's Tabazadeh and Lin)

This was the main focus of this Cooperative Agreement and the results are contained in two published papers attached)

- 2 Utilization of satellite measurements of trace gases along with analysis of temperatures and dynamic conditions to understand ice cloud formation, dehydration and sedimentation in the winter polar regions. (Task 6 Dr Stone)

This was a specific task for Dr. Stone and resulted in a paper has been submitted for publication (attached)

3. Comparison of the HALOE and SAGE II time dependencies of the Pinatubo aerosol decay (Task 7, Dr. Bergstrom)

This was a specific task for Dr. Bergstrom and resulted in a paper that is being prepared for publication.

III. Publications:

1. Tabazadeh, A.S., Martin, S.T. and J.S. Lin, The effects of particle size and nitric acid uptake on the homogeneous freezing of sulfate aerosols. *Geophys. Res. Lett.*, 27, 1111 (2000).
2. Lin, J.S. and A. Tabazadeh, Parameterization of an Aerosol Physical Chemistry Model (APCM) for the $\text{NH}_3/\text{H}_2\text{SO}_4/\text{HNO}_3/\text{H}_2\text{O}$ system at cold temperatures, *J. Geophys. Res.*, 106, 4815-4829, (2001)
3. Stone, E.S., A. Tabazadeh, E. Jensen, H.C. Pumphrey, M.L. Santee and J. L. Mergenthaler, The onset, extent and duration of dehydration in the Southern Hemisphere polar vortex, *J. Geophys. Res.*, in press (2001)

IV Presentations

AGU99 Conference, San Francisco, CA USA, 13-17 December 1999

1. Tabazadeh, A.S., Martin, S.T., and J.S. Lin, The effect of Nitric Acid Uptake on Homogeneous Sulfate Freezing
2. J. Lin and A. Tabazadeh, Cirrus Nucleation from Mixed-phase Particles,

AGU2000 Conference, Boston MA USA Spring 2000

1. Lin, J.S, A Comparison of Liquid Aerosol Composition Models in the Lower Stratosphere

The effect of particle size and nitric acid uptake on the homogeneous freezing of aqueous sulfuric acid particles

Azadeh Tabazadeh

NASA Ames Research Center, Moffett Field, CA

Scot T. Martin

Department of Environmental Sciences and Engineering, University of North Carolina, Chapel Hill, NC

Jin-Sheng Lin

Bay Area Environmental Research Institute, San Francisco, CA

Abstract. Recent laboratory data on ice freezing from aqueous H_2SO_4 solutions are used to update our homogeneous ice freezing nucleation algorithm. The effect of particle size on the ice freezing process is demonstrated by calculating and comparing ice freezing curves for different size particles ranging from 0.2 to 4 micron in radius. Using the ice nucleation model we show that liquid water saturation is required above -44°C to activate submicron H_2SO_4 particles into cloud droplets. A thermodynamic model is used to show that the available laboratory data on ice freezing from ternary $\text{H}_2\text{SO}_4/\text{HNO}_3/\text{H}_2\text{O}$ solutions are insufficient to adequately address the effect of HNO_3 uptake on the homogeneous freezing of aqueous H_2SO_4 particles into ice.

Introduction

Ice clouds play important roles in Earth's climate [Ramanathan *et al.*, 1983] and chemistry Solomon [1990]. One mechanism that has been suggested to initiate ice cloud nucleation in the atmosphere is homogeneous freezing of aqueous H_2SO_4 solution droplets [Sassen and Dodd, 1989; DeMott *et al.*, 1994; Jensen *et al.*, 1994; Heymsfield and Miloshevich, 1995; Demott *et al.*, 1997]. However, the ice freezing process through this mechanism is complicated by the fact that a significant fraction of gas phase HNO_3 will partition into sulfate aerosols near the ice freezing point of the solution [Tabazadeh *et al.*, 1994; Carslaw *et al.*, 1994].

The ice freezing curve in aqueous H_2SO_4 droplets was recently measured by Koop *et al.* [1998]. The ice freezing temperatures determined by Bertram *et al.* [1996] for aqueous H_2SO_4 droplets, which we previously used to parameterize our ice nucleation model [Tabazadeh *et al.*, 1997 a, b], appear to be systematically too high [Koop *et al.*, 1998]. In addition, differential scanning calorimetry has recently been used to determine the ice freezing curve in aqueous HNO_3 and ternary $\text{H}_2\text{SO}_4/\text{HNO}_3/\text{H}_2\text{O}$ droplets [Chang *et al.*, 1999]. In this work we use recent laboratory measurements on ice freezing from binary and ternary solution droplets [Koop *et al.*, 1998; Chang *et al.*, 1999], along with new surface tension data on the aqueous H_2SO_4 system [Myhre *et al.*, 1998], to update our homogeneous ice freezing nucleation algorithm.

Model Update

Figure 1 shows critical ice saturations expected to nucleate ice in aqueous H_2SO_4 , HNO_3 and ternary $\text{H}_2\text{SO}_4/\text{HNO}_3/\text{H}_2\text{O}$ solutions as a function of the ambient water vapor pressure based on recent laboratory measurements. The data of Koop *et al.* [1998] and Bertram *et al.* [1996] show very different behaviors for the freezing of ice from aqueous H_2SO_4 solution droplets. The main objective of this paper is to update our ice nucleation model to agree with more recent measurements.

An interesting feature of Figure 1 is that the ice freezing curves for both aqueous H_2SO_4 and HNO_3 solution droplets are nearly identical. According to equilibrium model calculations [Tabazadeh *et al.*, 1994; Carslaw *et al.*, 1994], the ionic strengths of $\text{H}_2\text{SO}_4/\text{H}_2\text{O}$ and $\text{HNO}_3/\text{H}_2\text{O}$ at the same relative

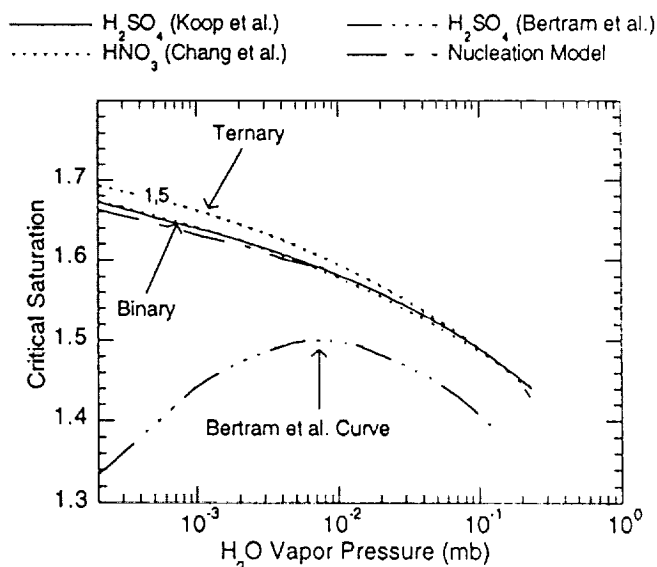


Figure 1. The variation of critical ice saturation as a function of water partial pressure over the solution. The solid and dotted curves are calculated directly from the tabulated relations given in Koop *et al.* [1998] and Chang *et al.* [1999]. The numbers on the dotted lines give the H_2SO_4 content of a ternary $\text{HNO}_3/\text{H}_2\text{SO}_4/\text{H}_2\text{O}$ aerosol in weight percent. The solid dotted curve is based on the data of Bertram *et al.* [1996] converted to an appropriate form using the method described in Tabazadeh *et al.* [1997a]. Also shown are the results of our ice nucleation model for a 4 micron aqueous H_2SO_4 particle.

humidity are similar in magnitude. Since the equilibrium freezing point depression is often directly proportional to the ionic strength, the fact that the two binary electrolytes have similar ice freezing kinetics is at least partially rationalized.

Also shown in Figure 1 are the ice freezing curves for $\text{H}_2\text{SO}_4/\text{HNO}_3/\text{H}_2\text{O}$ ternary solutions, which contain 1 and 5% H_2SO_4 by weight [Chang *et al.*, 1999]. The slight (< 2%) increase in the critical ice saturation in a ternary solution, as compared to the binary systems, is rationalized by the increase in entropy of the solution as a result of mixing. Below we use a thermodynamic model to show that the current laboratory data on ice freezing from ternary solutions are insufficient to adequately address the effect of HNO_3 uptake (by sulfate aerosols) on the ice formation process in the atmosphere.

Denoting V_d (cm^3) and w_s as the volume and weight percent of a H_2SO_4 solution droplet, the rate of ice nucleation (particle sec^{-1}) at a given temperature is:

$$J = C(T, w_s, V_d) \exp \left[\frac{-\Delta F_g(T, w_s) - \Delta F_{act}(T, w_s)}{kT} \right] \quad (1)$$

where C (particle sec^{-1}) is the preexponential factor, ΔF_g (ergs) is the Gibbs free energy for the formation of the ice germ, ΔF_{act} (ergs) is the diffusion activation energy of water molecules across the ice/sulfate solution phase boundary, and k is the Boltzmann constant. The preexponential factor and the Gibbs free energy are estimated as follows:

$$C(T, w_s, V_d) \equiv 2.1 \times 10^{33} V_d \sqrt{\sigma_{\text{sulf/ice}}(w_s, T) T} \quad (2)$$

$$\Delta F_g = \frac{4}{3} \pi \sigma_{\text{sulf/ice}} r_g^2 \quad (3)$$

where $\sigma_{\text{sulf/ice}}$ is the interface energy between the ice/sulfate solution and r_g (cm) is the critical germ radius. For our purposes, an ice freezing event occurs when $J = 1$ particle sec^{-1} .

We previously described [Tabazadeh *et al.*, 1997 a, b] how the equations (1) through (3) can be used to extract a numerical relation for the variation of activation free energy of water

molecules in solution based on laboratory ice freezing data. We follow the same procedure here to derive a new relation for the activation free energy of water molecules in solution based on the ice freezing data of Koop *et al.* [1998].

In deriving an expression for the activation free energy, we generated two fittings of the activation energy function for particle sizes of 1.55 and 6.3 micron in radius that bracket the laboratory size range [Koop *et al.*, 1998]. The final activation energy relation reported in Table 1 is obtained by averaging the two expressions above for different particle size assumptions. In addition, we replaced the surface tension relation in the model by a new expression based on recent laboratory measurements by Myhre *et al.* [1998]. All the functions required for the nucleation calculations are described and summarized in Table 1. The nucleation model calculates a unique solution for the ice freezing temperature of a given size droplet as a function of only the ambient water vapor pressure.

Atmospheric Implications

Figure 2 shows the effect of particle size on ice nucleation from an aqueous H_2SO_4 solution droplet. The size-dependence calculated by our model is in good agreement with the size-dependence measured in the laboratory for ice nucleation in pure supercooled water droplets (see Figure 2 in Pruppacher [1995]). As expected, due to smaller volumes (V_d term in equation 1), higher ice saturations are needed to form ice in submicron atmospheric particles as compared to micron-sized aerosols studied in the laboratory [Koop *et al.*, 1998]. Recent measurements [Chen *et al.*, 2000] support our calculations that submicron sulfate particles freeze at lower temperatures as compared to micron-sized particles.

Laboratory freezing data on submicron water droplets indicate that such droplets can often remain supercooled to temperatures near and sometimes below -40°C [Hagen *et al.*, 1981; Pruppacher, 1995]. Thus the fact that our ice nucleation model calculates a liquid water activation temperature below -40°C for submicron aqueous H_2SO_4 particles (Figure 2) is not surprising since the effect of solute is to further depress the freezing point of ice in solution beyond that of a pure supercooled water droplet. Overall, a nucleation model offers

Table 1. Ice Nucleation Functions

Latent heat of melting in erg mol^{-1} (T is in K): $L_m(T) = 10^7 [6005.2356 + 18.2719(T - 273.15) - 0.06354(T - 273.15)^2]$
Ice density (T is in K): $\rho_{\text{ice}}(T) = 0.916 - 8.75 \times 10^{-5}(T - 273.15) - 1.667 \times 10^{-7}(T - 273.15)^2$
Sulfate solution/air interface energy based on the data of Myhre <i>et al.</i> [1998] in dyn cm^{-1} (where w is the H_2SO_4 weight percent of the solution):
$\sigma_{\text{sulf/air}}^{180} = 85.75507114 + 9.541966318 \times 10^{-2}w - 1.103647657 \times 10^{-1}w^2 + 7.485866933 \times 10^{-3}w^3 - 1.912224154 \times 10^{-4}w^4 + 1.736789787 \times 10^{-6}w^5$
$\sigma_{\text{sulf/air}}^{220} = 82.01197792 + 5.312072092 \times 10^{-1}w - 1.050692123 \times 10^{-1}w^2 + 5.415260617 \times 10^{-3}w^3 - 1.145573827 \times 10^{-4}w^4 + 8.969257061 \times 10^{-7}w^5$
$\sigma_{\text{sulf/air}}^{260} = 77.40682664 - 6.963123274 \times 10^{-3}w - 9.682499074 \times 10^{-3}w^2 + 8.87979880 \times 10^{-4}w^3 - 2.384669516 \times 10^{-5}w^4 + 2.095358048 \times 10^{-7}w^5$
For $180 \leq T \leq 220$ K: $\sigma_{\text{sulf/air}}^T = \sigma_{\text{sulf/air}}^{220} + (5.5 - 0.025T)(\sigma_{\text{sulf/air}}^{180} - \sigma_{\text{sulf/air}}^{220})$
For $220 < T \leq 260$ K: $\sigma_{\text{sulf/air}}^T = \sigma_{\text{sulf/air}}^{260} + (6.5 - 0.025T)(\sigma_{\text{sulf/air}}^{220} - \sigma_{\text{sulf/air}}^{260})$
Diffusion activation energy $\times 10^{13}$ in ergs derived from the Koop <i>et al.</i> [1998] ice nucleation data (T is in K):
For $T < 220$ K: $\Delta F_{act} = -17459.516183 + 458.45827551T - 4.8492831317T^2 + 0.026003658878T^3 - 7.1991577798 \times 10^{-5}T^4$ $+ 8.9049094618 \times 10^{-8}T^5 - 2.4932257419 \times 10^{-11}T^6$
For $T > 220$ K: $\Delta F_{act} = 104525.93058 - 1103.76446517T + 1.0703327027T^2 + 0.017386254322T^3 - 1.5506854268 \times 10^{-6}T^4$ $- 3.2661912497 \times 10^{-8}T^5 + 6.467954459 \times 10^{-10}T^6$
Equilibrium sulfuric acid weight percent composition and water saturation vapor pressure: See Tabazadeh <i>et al.</i> [1997a]
Sulfuric acid solution density: See Myhre <i>et al.</i> [1998]

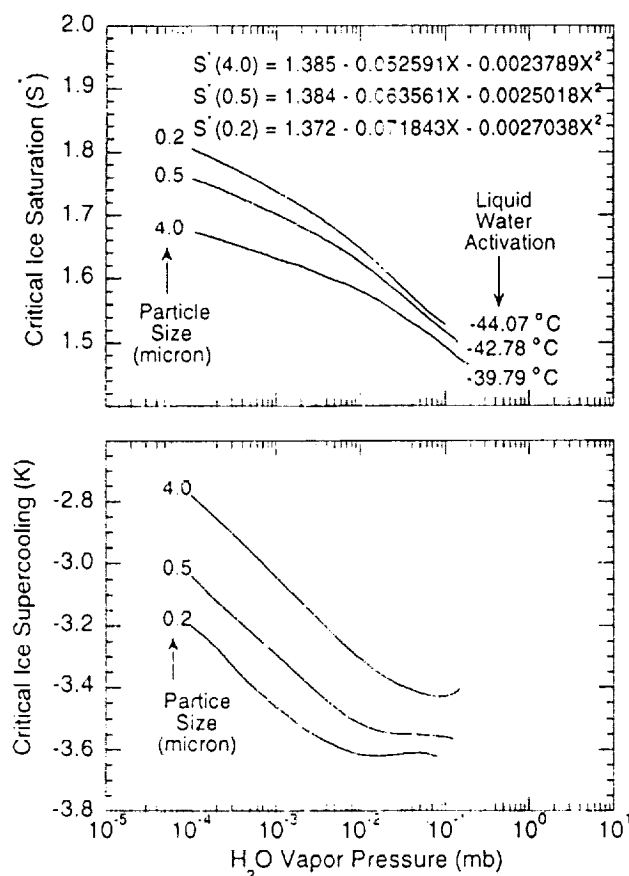


Figure 2. The variation of the critical ice saturation (and supercooling) as a function of water partial pressure and particle size in radius calculated using the ice nucleation model. The critical supercooling is defined as the difference between the critical ice freezing temperature and the ice frost point of the solution. Liquid water activation temperatures marked on the plot show transition temperatures above which particles activate into liquid water droplets prior to freezing into ice. The variable X in the above equation is $\ln(PH_2O)$, where PH_2O is the ambient water vapor pressure in mb.

several advantages compared to parameterizations for treating the ice formation process in the atmosphere. Simple parameterizations tend to provide information that is exclusive to one size particle, whereas in the atmosphere ice nucleation in principle occurs over an entire submicron aerosol particle size distribution.

Liquid water activation temperatures marked in Figure 2 (for three different particle sizes) show transition temperatures above which sulfate particles will first activate into liquid water droplets prior to freezing into ice. To accurately predict this transition point in the atmosphere is important since cirrus ice clouds that first go through a liquid water activation phase are often composed of a large population of small ice crystals [Jensen *et al.*, 1998]. Radiative properties of cirrus clouds are strongly affected by the number of ice particles nucleated [Jensen and Toon, 1994]. The results of our calculations show that submicron H_2SO_4 particles in the atmosphere can remain supercooled to temperatures near -44 °C. Therefore it is likely that above -44 °C cirrus ice clouds often form by first going through a liquid water activation phase provided that they are devoid of heterogeneous solid impurities [Martin, 1998; Demott *et al.*, 1997].

The composition of an aqueous H_2SO_4 solution droplet in the atmosphere is altered by the uptake of HNO_3 . In Figure 3 the change in the ternary solution composition as a function of temperature is shown for three selected water vapor pressure profiles, which bracket typical conditions in the lower stratosphere and upper troposphere. The shaded area shows the range of H_2SO_4 compositions of ternary systems for which the ice freezing properties of solutions have been determined in the laboratory [Chang *et al.*, 1999].

Ternary solution droplets containing between 1 to 5 wt % H_2SO_4 freeze at ice saturations near that of the binary systems [Chang *et al.*, 1999, see Figure 1]. In the background stratosphere the H_2SO_4 weight percent in solution near the ice nucleation point is located within the gray area for which the ice freezing properties of ternary solutions have been studied in the laboratory. Thus the effect of HNO_3 uptake in depressing the ice freezing temperature is negligible (Figure 1) if the stratosphere is in a background state (Figure 3). However, for a volcanically perturbed state, where H_2SO_4 mixing ratios are higher, the H_2SO_4 weight percent of a ternary solution near the ice freezing point is close to 15 % (Figure 3). Because this

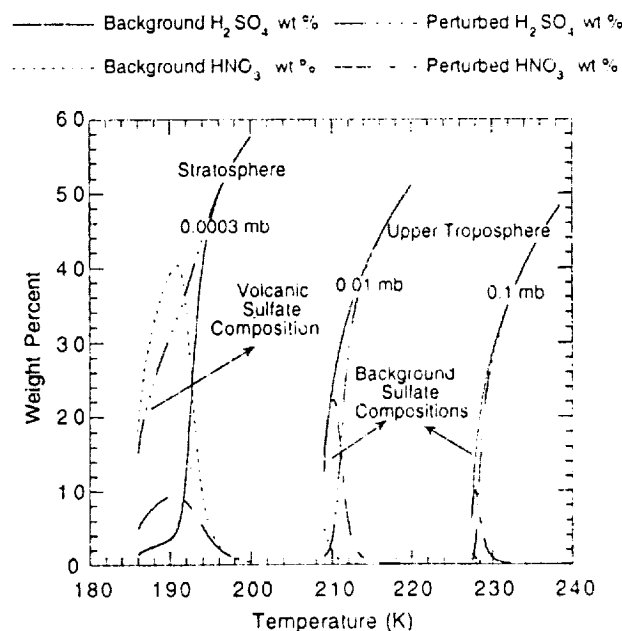


Figure 3. The variation of ternary $H_2SO_4/HNO_3/H_2O$ aerosol composition with temperature for different water vapor pressure regimes based on the thermodynamic relations given in Luo *et al.* [1995]. The 0.1 and 0.01 mb curves are calculated for a constant H_2SO_4 atmospheric mixing ratio of 100 ppt and variable HNO_3 atmospheric mixing ratios of 0.1 (background) and 2 ppt (perturbed by convective pollution) at 200 mb. The 0.0003 mb curves are calculated for a constant HNO_3 atmospheric mixing ratio of 10 ppb and variable H_2SO_4 mixing ratios of 0.5 (background) and 20 ppb (perturbed by volcanic eruptions) at 60 mb. The calculations were performed down to about -3.2 K below the equilibrium ice condensation point of the solution. The shaded area shows the range of H_2SO_4 compositions in ternary aerosol solutions for which the ice freezing properties of ternary systems have been measured in the laboratory [Chang *et al.*, 1999]. The arrows in the plot refer to H_2SO_4 composition in ternary solutions for which laboratory ice freezing data are lacking. Laboratory freezing data for ternary solutions are currently unavailable for volcanic and background conditions in the stratosphere and upper troposphere, respectively.

ternary composition regime has not been studied in the laboratory, it is difficult to compare and contrast the effect of HNO_3 uptake on the ice freezing process in the stratosphere between the two cases. Satellite data indicate that it may be more difficult to freeze aerosols in a volcanically perturbed environment as compared to a background state [Santee et al., 1998]. Thus additional laboratory data are needed to better understand how volcanic eruptions may affect the ice formation process in the lower stratosphere.

Similarly in the upper troposphere the laboratory data on ice freezing from ternary systems are insufficient to adequately describe and compare the differences between the background and perturbed states. For example, in a polluted upper troposphere HNO_3 mixing ratios reach values as high as 2 ppbv [Laaksonen et al., 1997; Schnieder et al., 1998]. The high levels of HNO_3 in the upper troposphere are linked to dry convection that injects polluted boundary layer air directly into the upper troposphere. The H_2SO_4 weight percent of ternary solutions in a polluted upper troposphere are located within the gray shaded area (see Figure 3). On the other hand, ice freezing curves for a background state (between 8 to 12% H_2SO_4 and 1 to 5 % HNO_3 by weight), containing about 100 pptv of HNO_3 , have not yet been explored in the laboratory (Figure 3). Thus it is difficult to address the question of how convection (leading to high levels of HNO_3) may affect cirrus formation in the upper troposphere when no information is available on ice freezing properties for compositions representative of the background state (~ 100 pptv of HNO_3).

Summary

We updated our homogeneous ice freezing nucleation code using recent laboratory measurements. Our results indicate that ice freezing curves for submicron aerosol particles are significantly different than those determined in the laboratory for micron-sized particles. Further we show that in the atmosphere, for temperatures above -44°C , submicron aqueous H_2SO_4 particles will activate into liquid water droplets prior to freezing into ice. Finally the available laboratory data on ice freezing from $\text{H}_2\text{SO}_4/\text{HNO}_3/\text{H}_2\text{O}$ solutions are insufficient to address how HNO_3 uptake by aqueous H_2SO_4 particles may affect the ice formation process in the atmosphere.

Acknowledgments. We thank N. Larsen and A. Ravishankara for helpful comments on the paper. We also thank Paul Demott and Luisa Molina for sending us preprints of their work on ice nucleation. This work was mainly supported by NASA's Atmospheric Chemistry Modeling and Analysis Program. AT and STM acknowledge support from Presidential Early Career Awards for Scientists and Engineers. STM is grateful for support received from the NSF Atmospheric Chemistry Program, the Petroleum Research Fund, and the Defense University Research Instrumentation Program. Send email to AT for a computer copy of the ice nucleation model.

References

- Bertram, A. K., D. D. Patterson, and J. J. Sloan, Mechanisms and temperature for the freezing of sulfuric acid aerosols measured by FTIR extinction spectroscopy, *J. Phys. Chem.*, **100**, 2376, 1996.
- Carlson, K. S., B. P. Luo, S. L. Clegg, T. Peter, P. Brimblecombe, and P. Crutzen, Stratospheric aerosol growth and HNO_3 gas phase depletion from coupled HNO_3 and water uptake by liquid particles, *Geophys. Res. Lett.*, **21**, 2479, 1994.
- Chang, H. A., T. Koop, L. T. Molina, and M. J. Molina, Phase transition in emulsified $\text{HNO}_3/\text{H}_2\text{O}$ and $\text{HNO}_3/\text{H}_2\text{SO}_4/\text{H}_2\text{O}$ solutions, *J. Phys. Chem.*, **103**, 2673-2679, 1999.
- Chen, Y., et al., Ice formation by sulfate and sulfuric acid particles under upper tropospheric condition, *J. Atmos. Sci.*, in press.
- DeMott, P. J., M. P. Meyers, and W. R. Cotton, Parameterization and impact of ice initiation processes relevant to numerical model simulations of cirrus clouds, *J. Atmos. Sci.*, **51**, 77, 1994.
- DeMott, P. J., D. C. Rogers, and S. M. Kreidenweis, The susceptibility of ice formation in the upper troposphere to insoluble aerosol components, *J. Geophys. Res.*, **102**, 19575, 1997.
- Hagen, D. E., R. J. Anderson, J. L. Kassner, Homogeneous condensation-freezing nucleation rate measurements for small water droplets in an expansion cloud chamber, *J. Atmos. Sci.*, **38**, 1236, 1981.
- Heymsfield, A. J., and L. M. Miloshevich, Relative humidity and temperature influences on cirrus formation and evolution: Observations from wave clouds and FIRE II, *J. Atmos. Sci.*, **52**, 4302, 1995.
- Jensen, E. J., O. B. Toon, D. L. Westphal, S. Kinne, and A. J. Heymsfield, Microphysical modeling of cirrus 1. Comparison with 1986 FIRE IFO measurements, *J. Geophys. Res.*, **99**, 10,421, 1994.
- Jensen, E. J., and O. B. Toon, Ice nucleation in the upper troposphere: Sensitivity to aerosol number density, temperature, and cooling rate, *Geophys. Res. Lett.*, **18**, 2019, 1994.
- Jensen, E., et al., Ice nucleation processes in upper tropospheric wave-clouds observed during SUCCESS, *Geophys. Res. Lett.*, **25**, 1367, 1998.
- Koop, T. H. P., Ng, L. T., Molina, M. J., Molina, A new optical technique to study aerosol phase transition: The nucleation of ice from H_2SO_4 aerosols, *J. Phys. Chem.*, **102**, 8924, 1998.
- Laaksonen, A., J. Hienola, M. Kulmala, and F. Arnold, Supercooled cirrus clouds formation modified by nitric acid pollution of the upper troposphere, *Geophys. Res. Lett.*, **24**, 3009, 1997.
- Luo, B., et al., Vapor pressures of $\text{H}_2\text{SO}_4/\text{HNO}_3/\text{HCl}/\text{HBr}/\text{H}_2\text{O}$ solutions to low stratospheric temperatures, *Geophys. Res. Lett.*, **22**, 247, 1995.
- Martin, S. T., Phase Transformation of the ternary system $(\text{NH}_4)_2\text{SO}_4\text{-H}_2\text{SO}_4\text{-H}_2\text{O}$ and the implications for cirrus cloud formation, *Geophys. Res. Lett.*, **25**, 1657, 1998.
- Mlyre, C. E. L., C. J. Nielsen, and O. W. Sasstad, Density and surface tension of aqueous H_2SO_4 at low temperatures, *J. Chem. Eng. Data*, **33**, 617, 1988.
- Pruppacher, H. R., A new look at homogenous ice nucleation in supercooled water drops, *J. Atmos. Sci.*, **52**, 1924, 1995.
- Ramanathan, V., E. J. Pitcher, R. C. Malone and L. Blackman, The response of a spectral general circulation model to refinements in radiative processes, *J. Atmos. Sci.*, **40**, 605, 1983.
- Santee, M. L., A. Tabazadeh, G. L. Manney, R. J. Salawitch, L. Froidevaux, W. G. Read, and J. W. Waters, UARS MLS HNO_3 observations: Implications for Antarctic PSCs, *J. Geophys. Res.*, **103**, 13,285, 1998.
- Sassen, K., and G. C. Dodd, Haze particle nucleation simulations in cirrus clouds, and applications for numerical and lidar studies, *J. Atmos. Sci.*, **46**, 3005, 1989.
- Schnieder, J., et al., Nitric acid (HNO_3) in the upper troposphere and lower stratosphere at mid latitudes: New results from aircraft-based mass spectrometric measurements, *J. Geophys. Res.*, **103**, 25,337, 1998.
- Solomon, S., Progress towards a quantitative understanding of Antarctic ozone depletion, *Nature*, **347**, 1990.
- Tabazadeh, A., R. P. Turco, K. Drlla, M. Z. Jacobson, and O. B. Toon, A study of Type I polar stratospheric cloud formation, *Geophys. Res. Lett.*, **21**, 1619, 1994b.
- Tabazadeh, A., E. Jensen, and O. B. Toon, A model description for cirrus cloud nucleation from homogeneous freezing of sulfate aerosols, *J. Geophys. Res.*, **102**, 23,845, 1997a.
- Tabazadeh, A., O. B. Toon, and E. Jensen, Formation and implications of ice particle nucleation in the stratosphere, *Geophys. Res. Lett.*, **24**, 2007, 1997b.
- J. Lin, NASA Ames Research Center, MS 245-4, Moffett Field, CA 94035-1000 (lin@sky.arc.nasa.gov).
- S. Martin, University of North Carolina at Chapel Hill, Chapel Hill, NC 27599-7400 (scot_martin@unc.edu).
- A. Tabazadeh, NASA Ames Research Center, MS 245-4, Moffett Field, CA 94035-1000 (atabazadeh@mail.arc.nasa.gov).

(Received August 2, 1999; Revised January 25, 2000; Accepted February 24, 2000)

A parameterization of an aerosol physical chemistry model for the $\text{NH}_3/\text{H}_2\text{SO}_4/\text{HNO}_3/\text{H}_2\text{O}$ system at cold temperatures

Jin-Sheng Lin

Bay Area Environmental Research Institute, San Francisco, California

Azadeh Tabazadeh

NASA Ames Research Center, Moffett Field, California

Abstract. Simple expressions are fitted to the results obtained from ion interaction thermodynamic models for calculating HNO_3 and H_2O vapor pressures over the $\text{NH}_3/\text{H}_2\text{SO}_4/\text{HNO}_3/\text{H}_2\text{O}$ system at cold temperatures. The vapor pressure expressions are incorporated into a mass conserving equilibrium solver for computing aerosol compositions in the lower stratosphere and upper troposphere. The compositions calculated from the aerosol physical chemistry model (APCM) are compared against previous parameterizations. The APCM compositions are in better agreement with the compositions obtained from ion interaction models than from other previous formulations of the $\text{NH}_3/\text{H}_2\text{SO}_4/\text{HNO}_3/\text{H}_2\text{O}$ system. The only advantage of the APCM over the ion interaction approach is that the numerical scheme used in the model is fast and efficient for incorporation into large-scale models. The APCM is used to calculate HNO_3 solubility in ammoniated aerosols as a function of HNO_3 , H_2SO_4 and NH_3 mass loadings in the lower stratosphere and upper troposphere. While the uptake of HNO_3 by ammoniated aerosols is strongly dependent upon the solution neutrality (or pH), we find that in both the lower stratosphere and upper troposphere a significant fraction of HNO_3 will exist in aerosol solutions near and below the ice frost point irrespective of solution neutrality.

1. Introduction

Thermodynamic electrolyte models are often used for calculating properties of inorganic aerosols in the lower troposphere [Stelson and Seinfeld, 1981; Pilinis and Seinfeld, 1987; Wexler and Seinfeld, 1991; Kim and Seinfeld, 1995; Jacobson *et al.*, 1996; Jacobson, 1999b] and stratosphere [Tabazadeh *et al.*, 1994; Carslaw *et al.*, 1994, 1995b; Weisenstein *et al.*, 1997]. In the lower troposphere, aerosol models are often used in air quality studies to assess the effects of aerosols on health, gas-phase partitioning, and visibility. In the stratosphere, aerosol models have been used to simulate the formation and growth of polar stratospheric clouds, which are linked to stratospheric ozone depletion [Solomon, 1999]. However, thermodynamic treatments in large-scale atmospheric models are in general not suited for calculating aerosol compositions in the upper troposphere. Since upper tropospheric aerosols participate in the nu-

cleation and growth of cirrus clouds and may also be involved in the scavenging of trace gas species, it is important to understand their chemical and physical properties [Kärcher and Solomon, 1999].

Recently, equilibrium aerosol formulations have been incorporated into three-dimensional models to simulate the radiative impacts of aerosols on climate [Adams *et al.*, 1999; Jacobson, 2000]. In this work, an aerosol physical chemistry model (APCM) with an efficient solving scheme suitable for incorporation into large-scale atmospheric models is developed. The APCM is compared against various parameterizations, including results from the aerosol inorganics model (AIM2) of Clegg *et al.* [1998a].

2. Background on Thermodynamic Aerosol Models

2.1. Ion Interaction Approach

The ion interaction approach is originally based on the work of Pitzer [1991]. The solution behavior in Pitzer's method is determined by a series of single-ion (and water) activity equations that are based on

Table 1. A_n Coefficients for the Vapor Pressure of HNO_3^a

r	a_0	a_1	a_2	a_3	a_4	a_5	a_6	a_7
0.0	12.6923	-0.0325979	-0.071719	0.812331	2.34482	0.000438486	-0.00428908	-0.000709075
0.1	12.4691	-0.0019955	-0.077484	0.727085	2.42858	0.000259723	-0.00442994	-0.000706633
0.2	12.2326	0.0260933	-0.085355	0.644593	2.52519	9.32848e-05	-0.00453571	-0.000694942
0.3	11.9840	0.0513596	-0.094561	0.567113	2.63058	-5.53402e-05	-0.00461276	-0.000678339
0.4	11.7205	0.0725417	-0.104727	0.500403	2.74278	-0.000172282	-0.00466394	-0.000659102
0.5	11.4289	0.0950553	-0.116820	0.450799	2.86783	-0.000241534	-0.00468708	-0.000632214
0.6	11.0837	0.0953196	-0.134271	0.415462	3.02666	-0.000267273	-0.00467490	-0.000579027
0.7	10.6697	0.106923	-0.160517	0.378195	3.24022	-0.000284624	-0.00461980	-0.000480710
0.8	10.2087	0.117295	-0.194708	0.324242	3.50279	-0.000327867	-0.00451884	-0.000342092
0.9	9.73753	0.130202	-0.232997	0.251054	3.79040	-0.000406493	-0.00437409	-0.000184569
1.0	9.28445	0.144365	-0.271608	0.165018	4.07962	-0.000510598	-0.00418932	-2.90206e-05
1.1	8.87335	0.156600	-0.306440	0.080649	4.34517	-0.000611458	-0.00396949	0.000101871
1.2	8.55964	0.157392	-0.327751	0.039034	4.52665	-0.000618013	-0.00372273	0.000153819
1.3	8.33474	0.134427	-0.331971	0.092212	4.60197	-0.000411043	-0.00345255	0.000106943
1.4	7.95881	0.110127	-0.354342	0.142888	4.78919	-0.000208202	-0.00313268	0.000158658
1.5	7.51749	0.0956133	-0.390173	0.143658	5.05815	-0.000120908	-0.00275735	0.000282545
1.6	7.14929	0.0860305	-0.421553	0.118501	5.29796	-0.000104343	-0.00234767	0.000379673
1.7	6.88502	0.0761817	-0.441786	0.092775	5.46818	-0.000107787	-0.00192436	0.000413991
1.8	6.68262	0.0630763	-0.453078	0.080818	5.58436	-0.000101314	-0.00149773	0.000397780
1.9	6.43124	0.0455338	-0.465952	0.086457	5.71507	-7.48198e-05	-0.00106043	0.000386668
2.0	5.72588	0.0242624	-0.524014	0.096528	6.13955	-5.31470e-05	-0.00053951	0.000609824
∞^b	11.5869	0.222271	-0.109389	0.279027	2.83237	-0.00101574	-0.00488557	-0.000704950

^a $A_n = a_0 + a_1 w_1 + a_2 w_2 + a_3 \sqrt{w_1} + a_4 \sqrt{w_2} + a_5 w_1^2 + a_6 w_1 w_2 + a_7 w_2^2$.

^b The ∞ represents the ternary system of $\text{NH}_3/\text{HNO}_3/\text{H}_2\text{O}$ (i.e., $\text{H}_2\text{SO}_4 = 0$).

thermodynamic properties of mixed solutions. Physical parameters for the fundamental activity relations in an ion interaction model are fitted to laboratory measurements of solute-water mixtures of interest. Thermodynamic electrolyte models based on the ion interaction approach have evolved significantly in recent years by Clegg and coworkers [e.g., Clegg and Brimblecombe, 1990, 1995a, 1995b; Carslaw et al., 1995a; Clegg et al., 1998a, 1998b]. Since the models of Clegg and coworkers, collectively referred to as aerosol inorganics model (AIM2), are fitted to laboratory measurements conducted over a broad temperature range (< 200 to 328°K), they are more accurate than those based on the common binary activity approach described in section 2.2. However, the complex nature of the ion interaction approach makes AIM2 computationally impractical for three-dimensional applications. Here we use AIM2 to generate solution compositions and vapor pressures for the $\text{NH}_3/\text{H}_2\text{SO}_4/\text{HNO}_3/\text{H}_2\text{O}$ system for a wide range of humidities and temperatures.

2.2. Binary Activity Approach

The second approach first emerged from modeling inorganic aerosols in air quality studies [e.g., Stelson and Seinfeld, 1981; Bassett and Seinfeld, 1983; Saxena et al., 1986]. This method separates out water (via

either the Gibbs-Duhem equation or the water equation [Stokes and Robinson, 1966]) and solute activity coefficients. Usually, a mixing rule of either Bromley [1973] or Kusik and Meissner [1978] is used to estimate the mixed solute activity coefficients. The equilibrium models based on this approach require only a knowledge of water and solute activity coefficients at a binary level. Thermodynamic models based on the binary activity approach are computationally more efficient but less accurate than the ion interaction approach because the physics of the activity coefficients in the former approach are mainly based on the behavior of binary solutions instead of mixed solution properties used in the latter formulations. To contrast two different thermodynamic treatments, we will update an equilibrium model based on the binary activity approach, EQUISOLV II [Jacobson et al., 1996; Jacobson, 1999b], and compare its predictions against results obtained from AIM2. EQUISOLV II applies a well-converged numerical solver scheme to simultaneously solve a large number of equilibrium equations.

2.3. Vapor Pressure Approach

A combination of the two approaches outlined in sections 2.1 and 2.2 is used in this work to develop a fast and accurate parameterization of the $\text{NH}_3/\text{H}_2\text{SO}_4/$

Table 2. B_n Coefficients for the Vapor Pressure of HNO_3^a

r	b_0	b_1	b_2	b_3	b_4	b_5	b_6	b_7
0.0	-7672.46	67.7280	32.3655	-259.196	-235.30	-0.256884	0.97336	0.197376
0.1	-7609.77	50.7068	32.9809	-222.190	-255.43	-0.131368	1.07699	0.201805
0.2	-7541.22	35.7444	34.4801	-189.780	-280.54	-0.026085	1.16451	0.202182
0.3	-7467.24	22.7871	36.6718	-162.151	-309.62	0.059118	1.23812	0.199536
0.4	-7387.11	11.9765	39.4988	-140.155	-342.40	0.122744	1.29896	0.194190
0.5	-7297.89	3.4748	43.2297	-124.533	-380.56	0.163341	1.34688	0.184702
0.6	-7194.29	-3.0516	48.6478	-113.773	-428.87	0.184446	1.38064	0.166777
0.7	-7074.27	-8.6193	56.4190	-103.509	-491.39	0.196255	1.39907	0.136740
0.8	-6944.62	-14.0870	66.1301	-90.235	-565.46	0.207582	1.40222	0.096867
0.9	-6815.18	-19.5849	76.6808	-73.739	-644.27	0.220387	1.39134	0.053245
1.0	-6693.25	-24.6807	87.0206	-56.230	-721.33	0.231211	1.36800	0.011651
1.1	-6584.97	-28.3719	96.0022	-42.304	-789.58	0.230911	1.33398	-0.021582
1.2	-6504.53	-27.8717	100.995	-44.004	-832.71	0.192747	1.29170	-0.031795
1.3	-6449.42	-19.3426	100.908	-77.488	-843.95	0.079582	1.24188	-0.012861
1.4	-6347.58	-8.4904	106.038	-117.723	-886.93	-0.052980	1.17584	-0.022354
1.5	-6203.79	-0.1957	118.040	-143.506	-971.43	-0.156090	1.08786	-0.069346
1.6	-6055.69	4.3272	133.047	-152.440	-1073.17	-0.221191	0.98027	-0.132468
1.7	-5927.18	6.5545	148.101	-146.787	-1173.72	-0.249961	0.85834	-0.195765
1.8	-5829.77	6.2290	161.504	-129.145	-1262.57	-0.245338	0.72779	-0.250386
1.9	-5768.38	3.1411	172.326	-101.381	-1334.05	-0.209351	0.59425	-0.291726
2.0	-5744.66	-2.5250	180.115	-63.965	-1385.49	-0.141562	0.46318	-0.317848
∞^b	-7298.14	-51.7642	35.6176	-55.070	-360.093	0.376735	1.41665	0.252861

$$^a B_n = b_0 + b_1 w_1 + b_2 w_2 + b_3 \sqrt{w_1} + b_4 \sqrt{w_2} + b_5 w_1^2 + b_6 w_1 w_2 + b_7 w_2^2.$$

b The ∞ represents the ternary system of $\text{NH}_3/\text{HNO}_3/\text{H}_2\text{O}$ (i.e., $\text{H}_2\text{SO}_4 = 0$).

$\text{HNO}_3/\text{H}_2\text{O}$ system for atmospheric applications. The vapor-pressure approach requires generation of large sets of H_2O and HNO_3 vapor pressure arrays over the $\text{NH}_3/\text{H}_2\text{SO}_4/\text{HNO}_3/\text{H}_2\text{O}$ system for many assumed compositions and temperatures. The vapor pressure, composition, and temperature fields generated are fitted into simple mathematical expressions similar to those derived by Luo *et al.* [1995] for the $\text{H}_2\text{SO}_4/\text{HNO}_3/\text{H}_2\text{O}$ system. The vapor pressure relations are then inserted into a numerical mass-conserving equilibrium solver similar to that used in EQUISOLV II [Jacobson *et al.*, 1996] for gas-aerosol phase partitioning calculations.

3. Model Development

3.1. Aerosol Physical Chemistry Model (APCM)

Luo *et al.* [1995] have shown that equilibrium partial pressures of HNO_3 and H_2O over the $\text{H}_2\text{SO}_4/\text{HNO}_3/\text{H}_2\text{O}$ system roughly follow a Clausius-Clapeyron relation of the form $\ln P = A + B/T$ (where P is pressure, T is temperature, and A and B are constants) for a fixed solution composition. For the quaternary system of $\text{NH}_3/\text{H}_2\text{SO}_4/\text{HNO}_3/\text{H}_2\text{O}$ we found a similar behav-

ior for the variation of HNO_3 and H_2O vapor pressures over the solution.

Assuming that NH_3 and H_2SO_4 reside completely in the condensed phase (i.e., both $\text{NH}_{3(g)}$ and $\text{H}_2\text{SO}_{4(g)}$ are negligible), we follow the approach of Luo *et al.* [1995] and define w_1 and w_2 as the weight percents of ammoniated sulfate and nitric acid, respectively, in the solution as follows:

$$w_1 = \text{weight \% of } (\text{NH}_4)_r\text{H}_{2-r}\text{SO}_{4(aq)},$$

$$w_2 = \text{weight \% of } \text{HNO}_{3(aq)}, \quad (1)$$

$$r = \frac{\text{NH}_3}{\text{H}_2\text{SO}_4} = \frac{\text{NH}_{4(aq)}^+}{\text{HSO}_{4(aq)}^- + \text{SO}_{4(aq)}^{2-}}, \quad (2)$$

where r in w_1 is the fixed mole ratio of ammonia to sulfuric acid, and (aq) is the aqueous-phase species. The r ratio can be considered as the degree of the ammoniated solution neutrality and can take on any values in APCM (including fractions) between 0.0 and 2.0. For example, if r equals 0.0, 1.0, and 2.0, w_1 represents the weight percents of H_2SO_4 , $(\text{NH}_4)\text{HSO}_4$, and $(\text{NH}_4)_2\text{SO}_4$, respectively, in the solution. Using Clegg *et al.*'s [1998a] model, we first generated a series of arrays of HNO_3 and H_2O vapor pressures for a wide range of weight percent

Table 3. C_w Coefficients for the Vapor Pressure of H_2O^a

r	C_0	C_1	C_2	C_3	C_4	C_5	C_6	C_7
0.0	22.7490	0.0424817	0.0533280	-0.0567432	-0.276555	-0.000621533	-0.000311769	-0.000283120
0.1	22.7669	0.0310031	0.0493720	-0.0270045	-0.265333	-0.000496930	-0.000261912	-0.000257919
0.2	22.7838	0.0223810	0.0457014	-0.0059721	-0.254223	-0.000403349	-0.000224673	-0.000234421
0.3	22.8005	0.0165207	0.0423183	0.0065020	-0.243407	-0.000339520	-0.000198990	-0.000212594
0.4	22.8179	0.0132215	0.0393297	0.0110504	-0.233647	-0.000303073	-0.000184277	-0.000192973
0.5	22.8367	0.0119853	0.0369883	0.0096303	-0.226435	-0.000288721	-0.000180339	-0.000177085
0.6	22.8556	0.0119008	0.0354244	0.0058633	-0.222617	-0.000287316	-0.000186497	-0.000165709
0.7	22.8706	0.0122336	0.0342757	0.0024714	-0.220187	-0.000291401	-0.000201103	-0.000156776
0.8	22.8791	0.0129460	0.0329580	-0.0009337	-0.215893	-0.000300122	-0.000221710	-0.000146949
0.9	22.8818	0.0143893	0.0311831	-0.0063234	-0.208231	-0.000316451	-0.000246179	-0.000134615
1.0	22.8812	0.0168823	0.0289977	-0.0153842	-0.197574	-0.000343217	-0.000273061	-0.000120122
1.1	22.8803	0.0204917	0.0267376	-0.0284821	-0.185921	-0.000381016	-0.000302055	-0.000105483
1.2	22.8846	0.0243030	0.0255578	-0.0417119	-0.179964	-0.000421023	-0.000333949	-9.75631e-05
1.3	22.8946	0.0259813	0.0267000	-0.0449953	-0.186824	-0.000440711	-0.000370519	-0.000103697
1.4	22.8950	0.0265182	0.0275800	-0.0428170	-0.191549	-0.000449334	-0.000409584	-0.000108446
1.5	22.8866	0.0275456	0.0272887	-0.0426774	-0.189011	-0.000462731	-0.000447757	-0.000106656
1.6	22.8752	0.0293967	0.0263037	-0.0461528	-0.182140	-0.000484748	-0.000483688	-0.000101242
1.7	22.8640	0.0319034	0.0251308	-0.0524783	-0.173920	-0.000514332	-0.000517346	-9.51958e-05
1.8	22.8542	0.0347733	0.0240901	-0.0603014	-0.166228	-0.000549028	-0.000549196	-9.03611e-05
1.9	22.8459	0.0376949	0.0233346	-0.0682171	-0.159987	-0.000586063	-0.000579624	-8.75512e-05
2.0	22.8381	0.0403666	0.0228641	-0.0749269	-0.155242	-0.000622692	-0.000608700	-8.66960e-05
∞^b	22.7279	0.0163541	0.0303799	-0.0208336	-0.151376	-0.000354967	-0.000653371	-0.000197299

^a $C_w = C_0 + C_1 w_1 + C_2 w_2 + C_3 \sqrt{w_1} + C_4 \sqrt{w_2} + C_5 w_1^2 + C_6 w_1 w_2 + C_7 w_2^2$.

^b The ∞ represents the ternary system of $NH_3/HNO_3/H_2O$ (i.e., $H_2SO_4 = 0$).

combinations (w_1, w_2 ; where $0.0\% \leq w_1 + w_2 \leq 85.0\%$) at cold temperatures, ranging from 180 to 270°K. The vapor pressures were then fitted into the following functions:

$$0.0\% \leq w_1 + w_2 \leq 85.0\%, \quad 180^\circ K \leq T \leq 270^\circ K, \quad (3)$$

$$\ln P_{HNO_3} = A_n(r, w_1, w_2) + \frac{B_n(r, w_1, w_2)}{T}, \quad (4)$$

$$\ln P_{H_2O} = C_w(r, w_1, w_2) + \frac{D_w(r, w_1, w_2)}{T}, \quad (5)$$

where P_{HNO_3} and P_{H_2O} are in mbar. Coefficients A_n , B_n , C_w , and D_w were then parameterized into a mathematical function of w_1 and w_2 similar to that described by Luo *et al.* [1995]. The fitting results are summarized in Tables 1-4 for different r ratios, ranging from 0.0 and 2.0 (r values are separated by an increment of 0.1).

In Plate 1 the calculated vapor pressures using equations (4) and (5) are compared with those obtained from AIM2 for three r ratios (shown in Plates 1a, 1b, and 1c). In general, P_{H_2O} calculated by equation (5) agrees well with the model of Clegg *et al.* [1998a]. However, the

agreement of P_{HNO_3} using equation (4) is rather poor for most compositions. As shown in Plate 1, the calculated P_{HNO_3} becomes increasingly inaccurate as the solution neutrality (i.e., r) increases. For some cases the difference between estimated P_{HNO_3} values and those predicted by AIM2 reached as high as a factor of 5. To ensure differences are minimized, Diff terms accounting for the differences (deviations) of the "calculated" values (estimated from equations (4) and (5)) and the "real" values (obtained from AIM2) were added to equations (4) and (5):

$$\ln P_{HNO_3} = A_n(r, w_1, w_2) + \frac{B_n(r, w_1, w_2)}{T} + \text{Diff}_n(r, w_1, w_2, T) \quad (6)$$

$$\ln P_{H_2O} = C_w(r, w_1, w_2) + \frac{D_w(r, w_1, w_2)}{T} + \text{Diff}_w(r, w_1, w_2, T). \quad (7)$$

For a fixed r , w_1 , and w_2 the Diff correction terms approximately follow simple polynomial functions in temperature:

$$\text{Diff}_n(r, w_1, w_2, T) = \sigma_{n0} + \sigma_{n1} T + \sigma_{n2} T^2 \quad (8)$$

Table 4. D_w Coefficients for the Vapor Pressure of H_2O^a

r	d_0	d_1	d_2	d_3	d_4	d_5	d_6	d_7
0.0	-5850.24	21.9744	1.48745	-44.5210	59.6400	-0.384362	-0.644671	-0.208556
0.1	-5849.94	19.8594	1.73322	-39.7129	58.0581	-0.336545	-0.606959	-0.210361
0.2	-5849.15	17.5776	1.92716	-34.3704	56.5456	-0.289409	-0.568784	-0.211815
0.3	-5848.04	15.1511	2.06677	-28.5548	55.1548	-0.243024	-0.530295	-0.212915
0.4	-5846.79	12.6262	2.12829	-22.4377	54.0535	-0.197733	-0.491539	-0.213544
0.5	-5845.48	10.1120	2.06175	-16.4657	53.5369	-0.154503	-0.452501	-0.213397
0.6	-5843.72	7.79449	1.85460	-11.3889	53.6970	-0.115030	-0.413300	-0.212396
0.7	-5840.63	5.79437	1.60810	-7.6468	53.9687	-0.0803938	-0.374279	-0.211123
0.8	-5835.71	4.05810	1.46205	-4.9098	53.5707	-0.0500282	-0.335935	-0.210378
0.9	-5829.33	2.44674	1.47151	-2.5108	52.2170	-0.0225318	-0.298645	-0.210471
1.0	-5822.28	0.84270	1.60302	0.0831	50.1179	0.0033213	-0.262577	-0.211194
1.1	-5815.44	-0.79036	1.74377	2.9989	47.9281	0.0280087	-0.227587	-0.211883
1.2	-5810.31	-2.20859	1.55496	5.1396	47.5949	0.0492844	-0.193207	-0.210535
1.3	-5807.19	-2.71615	0.62592	3.4557	51.4599	0.0605252	-0.158668	-0.204729
1.4	-5801.66	-2.43122	-0.39261	-1.5150	55.7388	0.0628630	-0.124306	-0.198357
1.5	-5792.68	-1.85557	-1.06065	-7.4818	57.9126	0.0612095	-0.091134	-0.193964
1.6	-5781.23	-1.28487	-1.31402	-13.0971	57.6578	0.0586697	-0.059876	-0.191880
1.7	-5768.33	-0.88563	-1.18923	-17.6257	55.2142	0.0571507	-0.030919	-0.191856
1.8	-5754.83	-0.75269	-0.74364	-20.6765	50.9331	0.0578653	-0.004421	-0.193536
1.9	-5741.30	-0.93290	-0.03072	-22.0791	45.1436	0.0615518	0.019549	-0.196612
2.0	-5728.09	-1.44363	0.91523	-21.7913	38.0640	0.0686466	0.040959	-0.200889
∞^b	-5736.70	-0.27462	2.02241	0.5073	20.6699	0.0337051	-0.045872	-0.179320

^a $D_w = d_0 + d_1 w_1 + d_2 w_2 + d_3 \sqrt{w_1} + d_4 \sqrt{w_2} + d_5 w_1^2 + d_6 w_1 w_2 + d_7 w_2^2$.

^b The ∞ represents the ternary system of $NH_3/HNO_3/H_2O$ (i.e., $H_2SO_4 = 0$).

$$\text{Diff}_w(r, w_1, w_2, T) = \sigma_{w0} + \sigma_{w1} T + \sigma_{w2} T^2. \quad (9)$$

where σ are second order polynomial coefficients fitted for a particular combination of w_1 , w_2 , and r . The effects of including Diff terms in improving the vapor pressure fits are shown in Plates 1d-1f where HNO_3 and H_2O vapor pressures calculated from equations (6) and (7) (with polynomial coefficients of equations (8) and (9)) are compared against AIM2 results for the same r ratios examined above. As shown in Plates 1d-1f, Diff terms force the calculated vapor pressures of both H_2O and HNO_3 to agree with AIM2 results. For r values other than 0.0, 1.0, and 2.0, including Diff terms in vapor pressure relations produces a nearly exact agreement with AIM2 results. Thus, for APCM we tabulated polynomial coefficients of σ (lookup tables available as electronic supporting material¹) for all possible combinations of w_1 , w_2 , and r . The weight percents of w_1 and

w_2 in the lookup tables cover and span the composition spectrum from 0.0% to 85.0% with 1% increments in composition.

As temperatures cool, solubilities of trace gases, such as nitric acid, increase significantly, thereby depleting gas phase concentrations. Thus it is essential to calculate the distribution of HNO_3 between the gas and aerosol phases. To simulate the gas-aerosol partitioning of HNO_3 , equations (6) and (7) are coupled with mass conservation of HNO_3 :

$$\text{total } HNO_3 = P_{HNO_3} + HNO_{3(aq)} \quad (\text{in mol/m}^3). \quad (10)$$

Three unknowns, $(NH_4)_r H_{2-r} SO_{4(aq)}$ (or w_1), $HNO_{3(aq)}$ (or w_2), and P_{HNO_3} , can be uniquely determined by equations (6), (7), and (10). For this work, the same numerical scheme as that utilized in EQUISOLV II [Jacobson *et al.*, 1996] is applied to solve equations (6)-(10) iteratively.

At iteration steps where w_1 and w_2 are not tabulated in the lookup tables, the bilinear (area weighted) averaging [Jacobson, 1999a] is adopted for interpolation. For example, to estimate properties at $[w_1, w_2] = [25.3, 10.8]$, results obtained from four adjacent points,

¹Supporting lookup tables are available via Web browser or via Anonymous FTP from ftp://kosmos.agu.org/directory/append/ (Username = "anonymous", Password = "guest"); subdirectories in the ftp site are arranged by paper number. Information on searching and submitting electronic supplements is found at http://www.agu.org/pubs/essup/about.html.

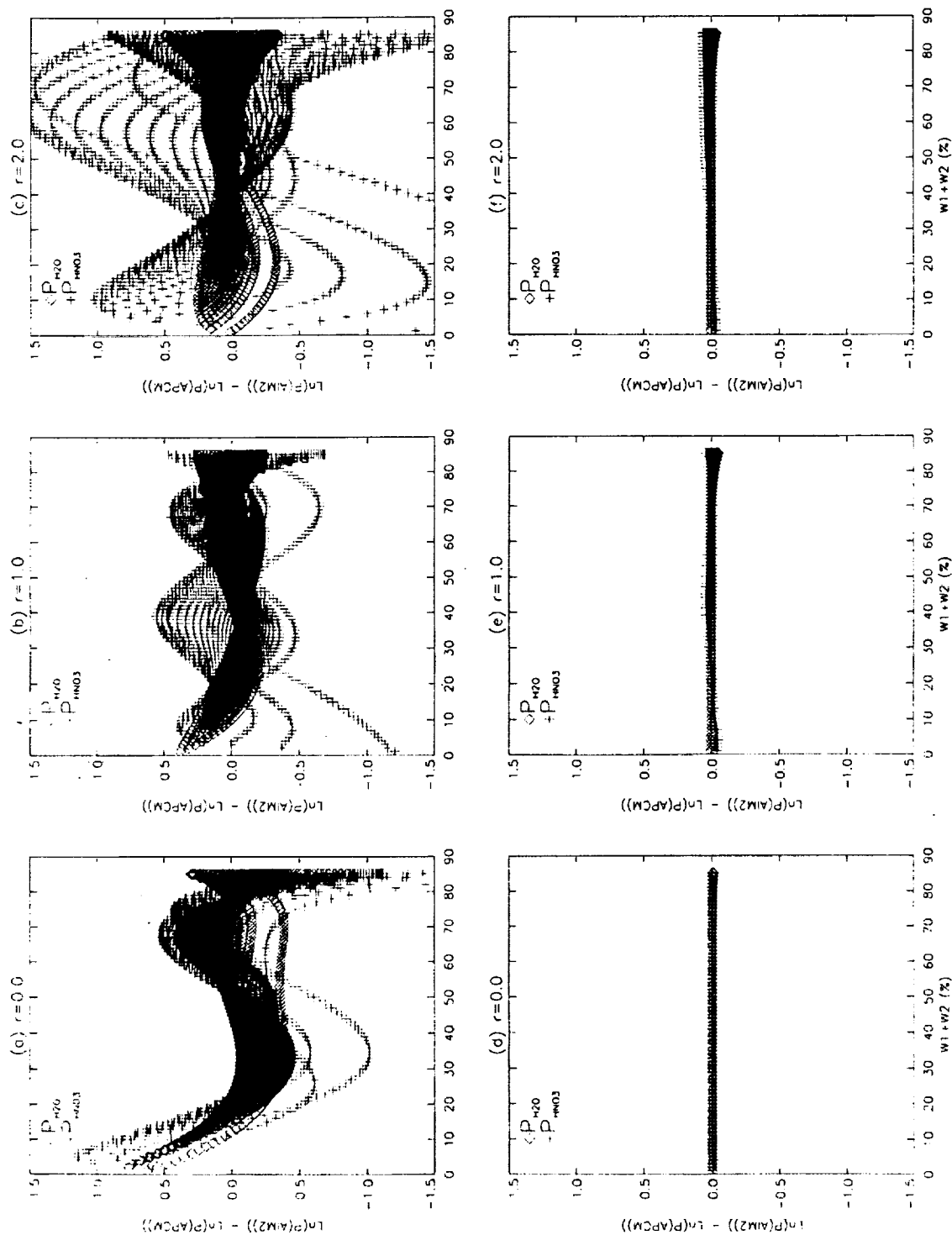


Plate 1. Comparison of vapor pressures obtained from APCM parameterization and those predicted by AIM2 for three r ratios. (a, b, c) Vapor pressures calculated by equations (4) and (5), and (d, e, f) results calculated by equations (6) and (7).

Table 5. Composition Functions^a

	A	B	C	D
$(NH_4)_2SO_4$				
$0.00 < a_w < 0.30$				
y_1	5.1229560233e+01	-9.6193408336e-01	1.4720578701e+02	-1.7229112367e-02
y_2	4.5462384945e+01	-9.4872028917e-01	3.3412155166e+02	-2.1124614825e+02
$0.30 \leq a_w < 0.60$				
y_1	9.7345916855e-01	-2.7444251275e+00	-1.8966528614e+01	1.9212056647e+01
y_2	1.0145647694e+00	-2.3916961554e+00	-2.2987950986e+01	2.1920018865e+01
$0.60 \leq a_w \leq 1.00$				
y_1	-5.3756389490e+02	1.3556456453e-02	-1.8951248281e+01	5.5692105238e+02
y_2	-4.2921431877e+02	1.2875856340e-02	-2.1275933520e+01	4.5075478762e+02
NH_4NO_3				
$0.00 < a_w < 0.40$				
y_1	1.3165236133e+02	-1.0103415600e+00	-3.1726829968e+01	-1.4042075761e+02
y_2	8.1149051028e+01	-9.6213385243e-01	1.0536766694e+02	-1.5360919227e+02
$0.40 \leq a_w < 0.85$				
y_1	8.5782004669e+01	-1.2795635979e+00	2.9982661442e+01	-1.0776290885e+02
y_2	3.2723371194e+01	-1.3299217851e+00	-8.1245973075e+00	-2.4520261799e+01
$0.85 \leq a_w \leq 1.00$				
y_1	-1.4969599516e-01	-2.0271382540e+01	-2.1065828892e+02	2.0679076661e+02
y_2	1.6636062187e+03	-1.3465428608e-01	1.8592287444e+02	-1.8496676635e+03
NH_4HSO_4				
$0.00 < a_w < 0.25$				
y_1	8.9145556445e+01	-9.2225449765e-01	2.1668157712e+02	-2.7552338531e+02
y_2	5.9840874514e+01	-9.3729948048e-01	2.7226224522e+02	-2.1721584622e+02
$0.25 \leq a_w < 0.80$				
y_1	2.8756459725e+00	-2.5507156109e+00	-3.3316860933e-01	-1.8494214012e-03
y_2	3.5550024880e+00	-2.0910350500e+00	-1.0492539829e+01	7.8923013513e+00
$0.80 \leq a_w \leq 1.00$				
y_1	-1.4227339985e+00	2.9277231432e+01	-1.7215058088e+01	1.8441662636e+01
y_2	-7.0483234774e-01	2.0832745270e+01	-2.3289593929e+01	2.3901137559e+01

^a $y = Aa_w^B + Ca_w + D$. Read 5.1229560233e+01 as 5.1229560233×10^1 . All parameterizations are valid for $190^\circ K \leq T \leq 260^\circ K$ only. Molality m is calculated by $m(a_w, T) = y_1(a_w) + (T - 190)[y_2(a_w) - y_1(a_w)]/70$, where a_w is water activity (relative humidity expressed in fraction). Composition functions for H_2SO_4 and HNO_3 in the same mathematical form are given by Tabazadeh et al. [1997a, 1997b].

[25.0, 10.0], [25.0, 11.0], [26.0, 10.0], [26.0, 11.0], are weighted and averaged, depending on how far the desired point is located away from the four fixed points. Similarly, a simple linear interpolation (of averaging predictions from two adjacent r ratios) is implemented if initial r falls inbetween the 0.1 increments (see Table 1). Since the intervals are small (1% for w_1 and w_2 and 0.1 for r), the two interpolation methods yield reasonable results that are in close agreement with AIM2 in predicting HNO_3 and H_2O vapor pressures over the $NH_3/H_2SO_4/HNO_3/H_2O$ system.

For conditions where H_2SO_4 mixing ratio is zero we define w_1 and w_2 as the weight percents of $NH_4NO_3(aq)$ and $HNO_3(aq)$, respectively, and repeat the above steps to obtain vapor pressures and solution compositions for the $NH_3/HNO_3/H_2O$ system.

3.2. An Update of EQUISOLV II

In addition to APCM parameterization an equilibrium model based on the binary activity approach [Stelson and Seinfeld, 1981; Pilinis and Seinfeld, 1987; Wexler and Seinfeld, 1991; Kim and Seinfeld, 1995; Jacobson et al., 1996; Jacobson, 1999b], EQUISOLV II [Jacobson et al., 1996; Jacobson, 1999b], is updated for application at colder temperatures. The updated EQUISOLV II will be compared against AIM2 and APCM. The important equilibrium equations to solve in EQUISOLV II for the $NH_3/H_2SO_4/HNO_3/H_2O$ system are

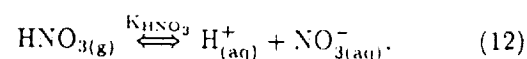
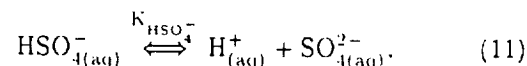
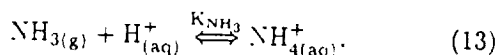


Table 6. Mean Binary Activity Coefficients^a

$\alpha_k(T) = \beta_0 + \beta_1 T + \beta_2 T^2$			
Coefficients	β_0	β_1	β_2
<i>HNO₃</i> (<i>n</i> =5)			
α_0	1.1550607531e+01	-8.6598065340e-02	1.6100335132e-04
α_1	-2.6045646534e+01	1.8570118152e-01	-3.4032931641e-04
α_2	9.6192566768e+00	-6.4314120728e-02	1.1363959743e-04
α_3	-1.4330104905e+00	9.3470490393e-03	-1.6321073928e-05
α_4	9.5181767818e-02	-6.1140131174e-04	1.0605856919e-06
α_5	-2.3568483179e-03	1.4936021604e-05	-2.5755879088e-08
<i>(NH₄)₂SO₄</i> (<i>n</i> =3)			
α_0	3.4428316946e+00	-4.5328321654e-02	1.0202137529e-04
α_1	-1.0030630804e+00	6.0339372495e-03	-1.2162329645e-05
α_2	4.2925175339e-02	-3.0262230896e-04	5.9904176768e-07
α_3	-6.6813265363e-04	5.0031688798e-06	-9.7460258587e-09
<i>NH₄NO₃</i> (<i>n</i> =4)			
α_0	2.7037375056e+00	-1.7880171498e-02	2.8497778393e-05
α_1	-4.9424685844e+00	2.1621849334e-02	-2.2789057453e-05
α_2	9.0584578176e-01	-4.2947161383e-03	4.7971905516e-06
α_3	-7.7554691781e-02	3.7618465057e-04	-4.3345626096e-07
α_4	2.4783745998e-03	-1.2123165585e-05	1.4181424491e-08
<i>NH₄HSO₄</i> (<i>n</i> =5)			
α_0	9.9601477451e-01	-1.1296951291e-02	1.7452716744e-05
α_1	1.4845831451e+00	-9.3756384679e-03	1.8989492030e-05
α_2	-2.9273249432e-01	1.3469653174e-03	-2.2718917359e-06
α_3	2.1988585949e-02	-8.1477260064e-05	1.0470356871e-07
α_4	-7.5397112432e-04	2.2096863963e-06	-1.6051821078e-09
α_5	9.7902066682e-06	-2.1560396221e-08	-3.3248336670e-12

^a $\ln \gamma = \sum_{k=0}^n \alpha_k(T) m^{k/2}$, Read 1.1550607531e+01 as 1.1550607531×10^1 . All parameterizations are valid for $190^\circ \text{K} \leq T \leq 260^\circ \text{K}$ only. Ion activity for the $\text{H}_2\text{SO}_4/\text{H}_2\text{O}$ system was not parameterized but instead tabulated in the computer codes.



where K_i is the equilibrium constant and (g) and (aq) refer to gas- and aqueous-phase species, respectively. The first dissociation step of H_2SO_4 ($\text{H}_2\text{SO}_{4(\text{l})} \rightarrow \text{HSO}_4^-_{(\text{aq})} + \text{H}^+_{(\text{aq})}$) is assumed to be complete.

Temperature-dependent water and solute activity coefficients in EQUISOLV II are modified at cold temperatures (190°K - 260°K) by parameterizing data from the model of Clegg *et al.* [1998a]. The temperature-dependent water activities of five electrolytes involved in equations (11)-(13), (H_2SO_4 , HNO_3 , $(\text{NH}_4)_2\text{SO}_4$, NH_4NO_3 , NH_4HSO_4) are improved in EQUISOLV II. For consistency with previous work by Tabazadeh *et al.* [1997a, 1997b] the binary solution compositions are parameterized into

$$m = y_1(a_w) + \frac{(T - 190)[y_2(a_w) - y_1(a_w)]}{70}, \quad (14)$$

where m is the molality of the binary electrolytes, a_w is the water activity (relative humidity expressed as fraction), and y is a function of a_w only (see Table 5). Mean binary activity coefficients (γ_{ij}^0) were parameterized by converting mole fraction activity coefficients (f) of Clegg *et al.*'s [1998a] model into molality base (γ) values according to equation (15), and using $\gamma_{ij}^0 = (\gamma_i^{\nu_+} \gamma_j^{\nu_-})^{\frac{1}{\nu_+ + \nu_-}}$ [Pitzer, 1991]:

$$f_i = \gamma_i \left(1 + \frac{M_w}{1000} \sum_k m_k \right), \quad (15)$$

where ν_+ and ν_- are the stoichiometric coefficients of the binary electrolytes (for example, $\nu_+ = 2$ and $\nu_- = 1$ for $(\text{NH}_4)_2\text{SO}_4$), M_w is the molecular weight of water, and summation is over all solute species. The mean activity coefficients were then fitted into simple polynomial functions (given in Table 6) of temperature and molality (where α_k and β_k are polynomial coefficients):

Table 7. Model Conditions^a

Cases	$r = \frac{\text{NH}_3}{\text{H}_2\text{SO}_4}$	NH ₃ , ppt	H ₂ SO ₄ , ppt	HNO ₃ , ppt	H ₂ O, ppm	Illustration
<i>Stratospheric Simulation ($P_{\text{total}} = 50 \text{ mbar}$)</i>						
Background	$r = 0.0$	0.0	500.0	10,000.0	5.0	Figure 1a and 1b
Volcanic	$r = 0.0$	0.0	20,000.0	10,000.0	5.0	Figure 2a and 2b
<i>Upper Tropospheric Simulation ($P_{\text{total}} = 200 \text{ mbar}$)</i>						
Background	$r = 0.0$	0.0	100.0	100.0	5.0, 50.0, 500.0	Figure 3a
	$r = 1.0$	100.0	100.0	100.0	5.0, 50.0, 500.0	Figure 3b
	$r = 2.0$	200.0	100.0	100.0	5.0, 50.0, 500.0	Figure 3c
Polluted	$r = 0.0$	0.0	100.0	2,000.0	5.0, 50.0, 500.0	Figure 4a
	$r = 1.0$	100.0	100.0	2,000.0	5.0, 50.0, 500.0	Figure 4b
	$r = 2.0$	200.0	100.0	2,000.0	5.0, 50.0, 500.0	Figure 4c
<i>HNO₃ Uptake ($P_{\text{total}} = 200 \text{ mbar}$)</i>						
Background	$r = 0.0 - 2.0$	0.0 - 200.0	100.0	100.0	5.0, 50.0, 500.0	Figure 5
	$r = \infty$	100.0	0.0	200.0	5.0, 50.0, 500.0	

^a P_{total} is total atmospheric pressure, and the mixing ratios used are atmospheric observations [Tabazadeh et al., 1998; Laaksonen et al., 1997].

$$\ln \gamma_{ij}^0 = \sum_{k=0}^n \alpha_k(T) m^{k/2}, \quad (16a)$$

$$\alpha_k(T) = \beta_0 + \beta_1 T + \beta_2 T^2. \quad (16b)$$

The above parameterizations induce relative errors of no more than a few percents for both water and solute activities. The largest errors occur at low molality regions where ion activities usually exhibit a com-

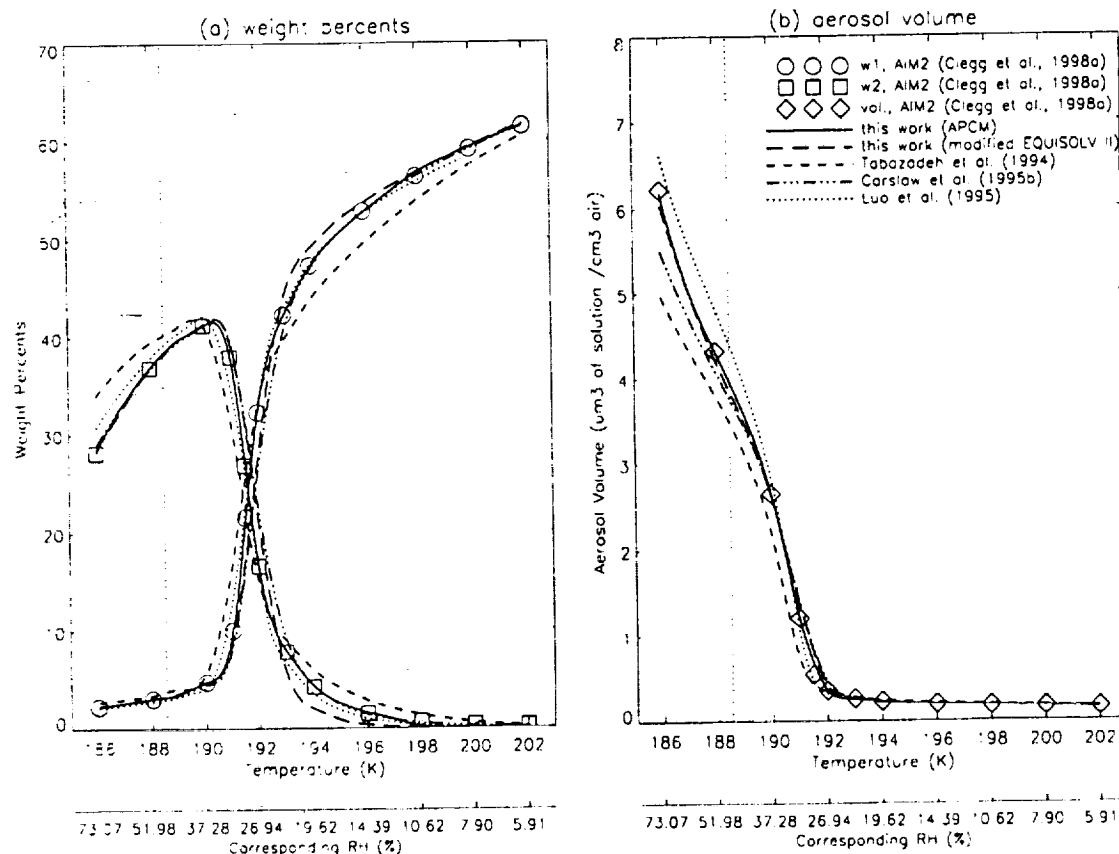


Figure 1. Comparison of various model predictions of (a) weight percents and (b) aerosol volume under background conditions in the stratosphere (see Table 7 for model conditions).

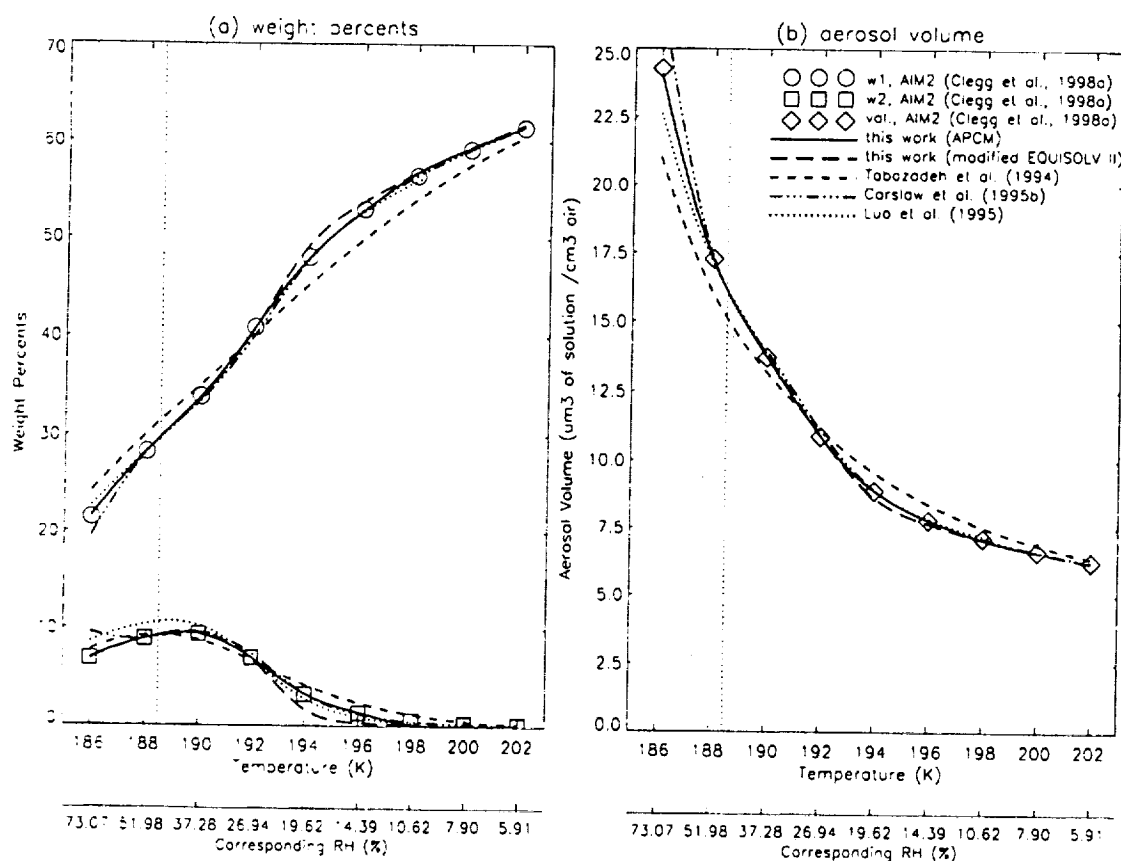


Figure 2. Comparison of various model predictions of (a) weight percents and (b) aerosol volume under volcanic conditions in the stratosphere (see Table 7 for model conditions).

plicated behavior. In addition to the improvement of binary water and solute activity coefficients, equilibrium constants of equations (11)–(13) were obtained from Clegg *et al.* [1998a] and converted into suitable molality-based units for use in EQUISOLV II. These modifications ensure perfect agreement of EQUISOLV II and AIM2 at a binary level where electrolyte solutions are made of H_2O plus only one electrolyte.

4. Model Intercomparison and Evaluation

4.1. $\text{H}_2\text{SO}_4/\text{HNO}_3/\text{H}_2\text{O}$

For the stratospheric system of $\text{H}_2\text{SO}_4/\text{HNO}_3/\text{H}_2\text{O}$, the compositions obtained from APCM are compared with previous formulations [Carslaw *et al.*, 1995b; Luo *et al.*, 1995; Tabazadeh *et al.*, 1994] under background and volcanic states (see Table 7 for model conditions used). Results from model intercomparisons between six different ternary aerosol models are shown in Figures 1 and 2. For the background stratosphere, APCM with Diff correction terms included is in good agreement with AIM2 [Carslaw *et al.*, 1995a]. The predicted weight percents by APCM overlap with AIM2 almost exactly throughout the entire temperature range shown in Figure 1a, whereas previous models deviate from

AIM2 either at the initial, in the middle, or at the final stage of aerosol growth (Figure 1b). Under volcanic conditions (H_2SO_4 increases from 0.5 to 20ppb), all models produce nearly identical results with only slight variations (Figures 2a and 2b).

4.2. $\text{NH}_3/\text{H}_2\text{SO}_4/\text{HNO}_3/\text{H}_2\text{O}$

In the upper troposphere, aerosol compositions are examined for both background and polluted states (see Table 7 for model conditions). Under polluted conditions, HNO_3 mixing ratios are elevated well beyond background values of 100ppt [Laaksonen *et al.*, 1997], mainly because of convective transport of polluted boundary layer air directly into the upper troposphere. Variations in the aerosol composition predicted by three models, APCM, modified EQUISOLV II (with the improved activity data), and AIM2 [Clegg *et al.*, 1998a], are illustrated in Figures 3 and 4. The points of ice saturation are marked as vertical dotted lines in Figures 3 and 4. For all cases studied and compared, APCM yields compositions that are in close agreement with AIM2. The modified EQUISOLV II with new activity data performs better in the regions where relative humidity (RH) is high. The deviations at lower relative humidity are likely caused by the uncertainties in mixed activity coefficients calculated from simple mix-

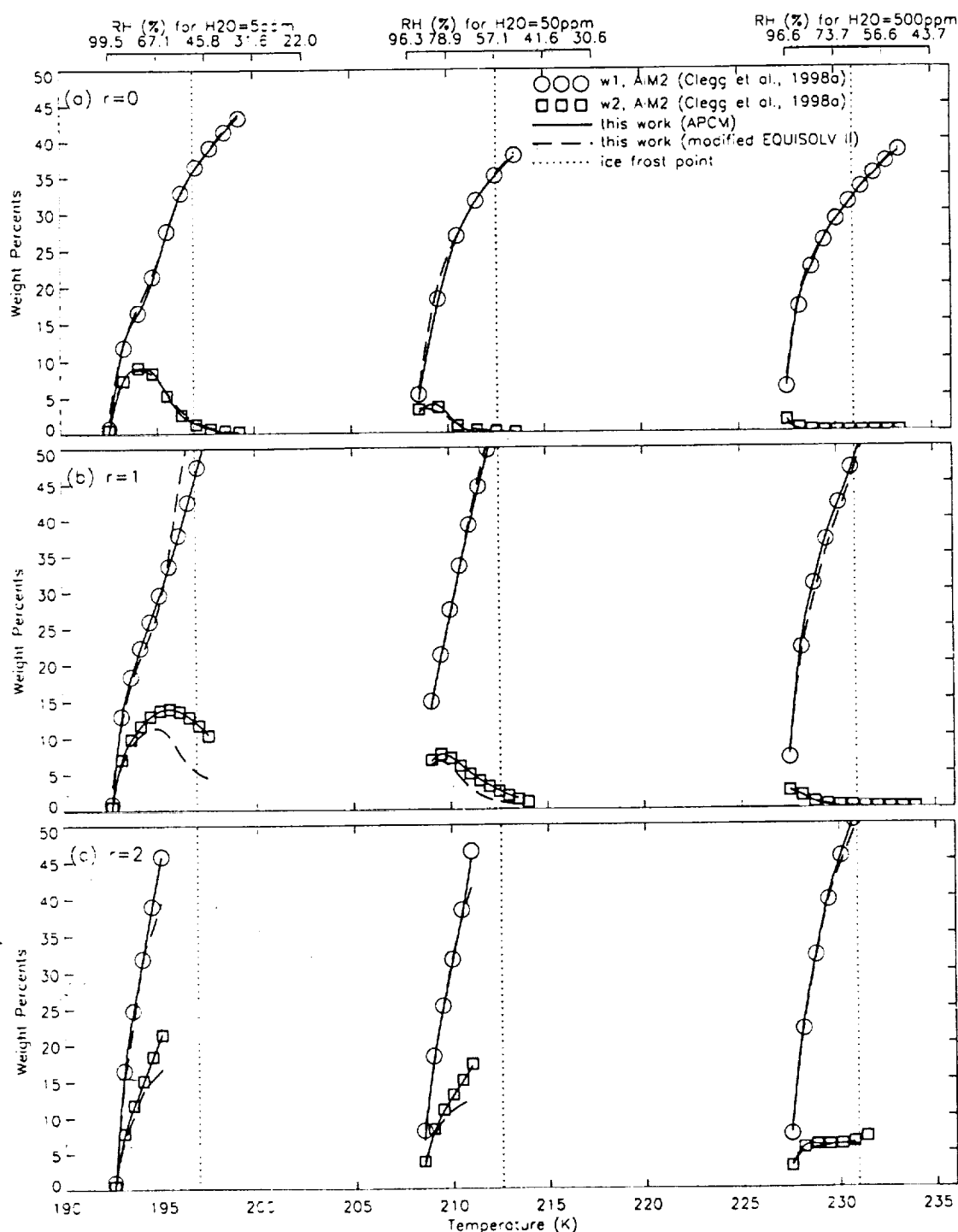


Figure 3. Variation of aerosol compositions as a function of temperature (or relative humidity) under background conditions in the upper troposphere (see Table 7 for model conditions). (a) $r = 0.0$, (b) $r = 1.0$, and (c) $r = 2.0$.

ing rules [Bromley, 1973; Kusik and Meissner, 1978] in EQUISOLV II.

We have also compared predicted molalities of individual components, NH_4^+ , H_2SO_4 ($= \text{HSO}_4^- + \text{SO}_4^{2-}$), and NO_3^- , in solution (instead of weight percents of w_1 and w_2) and found that the differences between APCM and AIM2 are no more than a few percent except at the very low or high solute concentration re-

gions. In other words, predictions by APCM are less accurate only in regions where weight percents approach the lower or upper limits (1% and 85%). Nevertheless, for very low weight percents, concentrations are too dilute to be significant, whereas for very high weight percents, relative humidities are sufficiently low that ammoniated salts, such as $(\text{NH}_4)_2\text{SO}_4$ or $(\text{NH}_4)_3\text{H}(\text{SO}_4)_2$ (letovicite), would most likely precipitate in solution

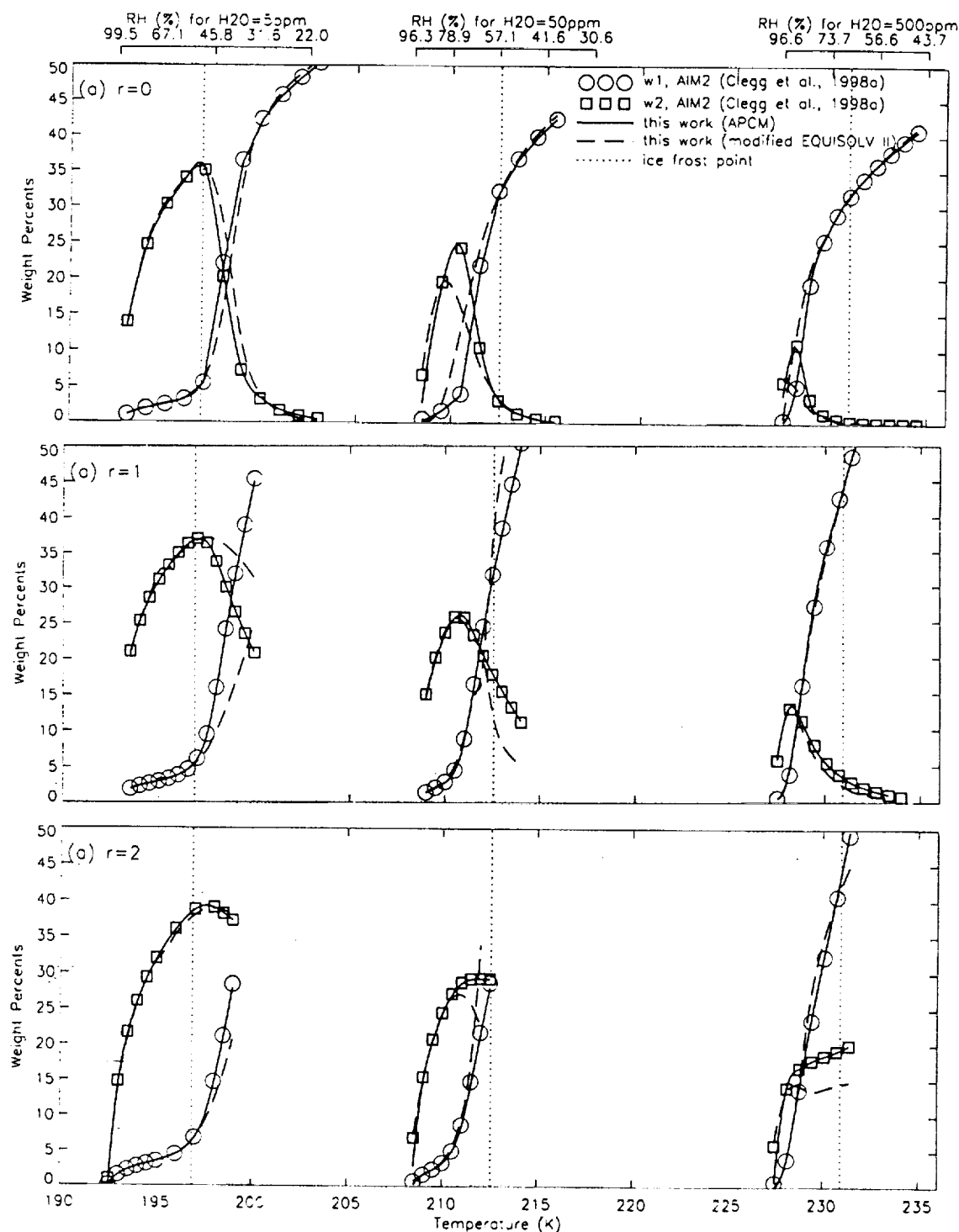


Figure 4. Variation of aerosol compositions as a function of temperature (or relative humidity) under polluted conditions in the upper troposphere (see Table 7 for model conditions). (a) $r = 0.0$. (b) $r = 1.0$, and (c) $r = 2.0$.

[Tabazadeh and Toon, 1998]. For example, crystallization of $(\text{NH}_4)_2\text{SO}_4$ occurs at $\sim 35\%$ RH at room temperature [Xu et al., 1998]. At colder temperatures, crystallization of $(\text{NH}_4)_2\text{SO}_4$ will probably occur at slightly higher RHs. In addition, for very concentrated solutions ($w_1 + w_2 > 85\%$), aerosol compositions predicted by AIM2 are often outside the range of model validation

[Clegg et al., 1998a]. For the reasons mentioned above, the limits imposed on the weight percents in the APCM are not a serious drawback. Also, as shown in Figures 3 and 4, the APCM compositions are most accurate near regions where ice reaches saturation in the atmosphere.

In addition to aerosol composition the APCM can be used to calculate the extent of HNO_3 uptake by up-

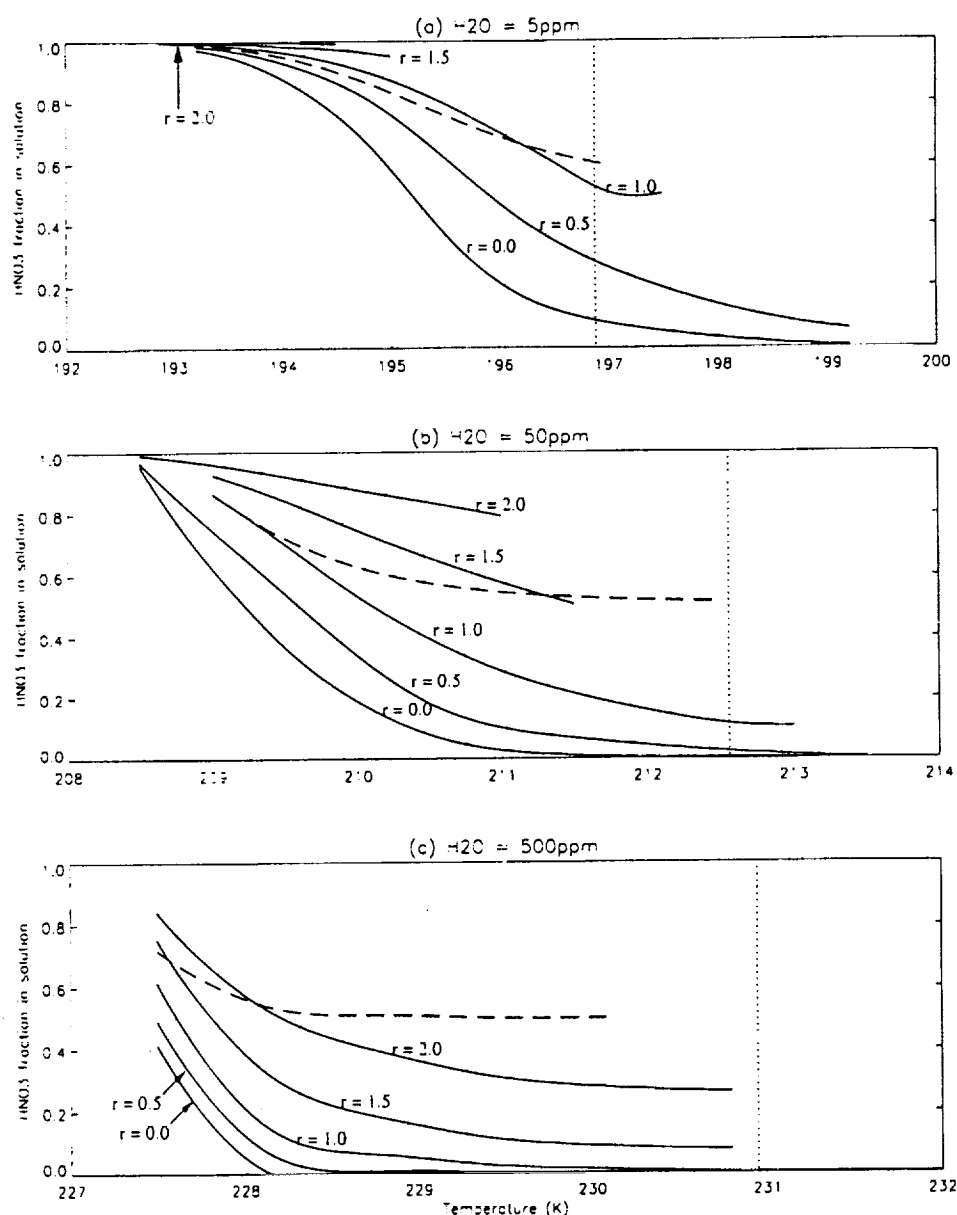


Figure 5. Uptake of HNO_3 in sulfate-based aerosols as a function of sulfate neutralization under background conditions in the upper troposphere (see Table 7 for model conditions). (a) $\text{H}_2\text{O} = 5\text{ppm}$, (b) $\text{H}_2\text{O} = 50\text{ppm}$, and (c) $\text{H}_2\text{O} = 500\text{ppm}$. (Dashed lines represent the uptake by pure NH_4NO_3 aerosols (i.e., $\text{H}_2\text{SO}_4 = 0$))

per tropospheric aerosols. Aircraft field experiments have shown that ammoniated particles are abundant in the upper troposphere [Talbot *et al.*, 1996, 1998; Tabazadeh *et al.*, 1998]. Here we examine how HNO_3 uptake may be affected by the presence of ammoniated aerosols in the upper troposphere. For simulations the H_2SO_4 and HNO_3 mixing ratios are fixed at background levels of 100 ppt each. NH_3 concentrations in the APCM are varied by increasing (or decreasing) r to account for changes in solution neutrality (or pH), ranging from pure H_2SO_4 solution droplets ($r = 0.0$) to fully ammoniated systems consisting of only $(\text{NH}_4)_2\text{SO}_4$ ($r = 2.0$) (see Table 7 for model conditions used).

In Figure 5, the uptake of HNO_3 , expressed as a fraction (i.e., ratio of concentration in the liquid phase to the total initial concentration), is shown for three different assumed water vapor pressure profiles. As expected, partitioning of HNO_3 in sulfate-based aerosols depends strongly on solution neutrality. In general, greater uptake occurs at lower temperatures and higher relative humidities. For example, at temperatures lower than 210°K (which corresponds to a relative humidity of 78% for $P_{\text{total}} = 200\text{mb}$ and $\text{H}_2\text{O} = 50\text{ppm}$), a significant fraction ($> 90\%$) of HNO_3 resides in fully neutralized ammoniated solutions, compared to only $< 20\%$ in the pure sulfate system (Figure 5b). It has been shown that

high levels of HNO_3 in solution may cause precipitation of ammoniated and/or nitrated salts, which could change the mode of ice formation from homogeneous to heterogeneous nucleation [Tabazadeh and Toon, 1998].

5. Conclusions

The ion interaction model of Clegg *et al.* [1998a] for the system of $\text{NH}_3/\text{H}_2\text{SO}_4/\text{HNO}_3/\text{H}_2\text{O}$ has been parameterized into a compact model well suited for incorporation into large-scale atmospheric models. The aerosol physical chemistry model (APCM) reproduces the AIM2 results of Clegg *et al.* [1998a] for a wide range of conditions in the upper troposphere and lower stratosphere. Model intercomparisons show that for the ternary system of $\text{H}_2\text{SO}_4/\text{HNO}_3/\text{H}_2\text{O}$ solution compositions obtained from APCM are in better agreement with those obtained from AIM2 than previous formulations. For the quaternary system of $\text{NH}_3/\text{H}_2\text{SO}_4/\text{HNO}_3/\text{H}_2\text{O}$, APCM results are also in good agreement with AIM2 predictions, particularly near the regions of ice saturation where the influence of ammoniated particles on the ice nucleation process is of interest. Extension of APCM to include other features such as calculations of deliquescence relative humidity and precipitation of solids in solution are under way.

Acknowledgments. This work is supported by NASA Atmospheric Chemistry Modeling and Analysis Program. A.T. acknowledges support from a Presidential Early Career Award for Science and Engineers. We thank Simon Clegg for many helpful discussions and for providing us with a computer code of the mixed electrolyte system. The AIM2 results in this work were obtained by running the "comprehensive" version of model II available at <http://www.uea.ac.uk/~e770/aim.html>. We are also grateful to Mark Jacobson for a copy of the EQUISOLV II and many helpful discussions. For a computer copy of the aerosol code and lookup tables send e-mail to lin@ice.arc.nasa.gov.

References

- Adams, P. J., J. H. Seinfeld, and D. M. Koch, Global concentrations of tropospheric sulfate, nitrate, and ammonium aerosol simulated in a general circulation model, *J. Geophys. Res.*, **104**, 13,791, 1999.
- Bassett, M., and J. H. Seinfeld, Atmospheric equilibrium model of sulfate and nitrate aerosols, *Atmos. Environ.*, **17**, 2237, 1983.
- Bromley, L. A., Thermodynamic properties of strong electrolytes in aqueous solutions, *AIChE J.*, **19**, 313, 1973.
- Carslaw, K. S., B. P. Luo, S. L. Clegg, T. Peter, P. Brimblecombe, and P. Crutzen, Stratospheric aerosol growth and HNO_3 gas phase depletion from coupled HNO_3 and water uptake by liquid particles, *Geophys. Res. Lett.*, **21**, 2479, 1994.
- Carslaw, K. S., S. L. Clegg, and P. Brimblecombe, A thermodynamic model of the system $\text{HCl}-\text{HNO}_3-\text{H}_2\text{SO}_4-\text{H}_2\text{O}$, including solubilities of HBr , from 328K to < 200K, *J. Phys. Chem.*, **99**, 11,557, 1995a.
- Carslaw, K. S., B. P. Luo, and T. Peter, An analytic expression for the composition of aqueous $\text{HNO}_3-\text{H}_2\text{SO}_4$ stratospheric aerosols including gas phase removal of HNO_3 , *Geophys. Res. Lett.*, **22**, 1877, 1995b.
- Clegg, S. L., and P. Brimblecombe, Equilibrium partial pressures and mean activity and osmotic coefficients of 0–100% nitric acid as a function of temperature, *J. Phys. Chem.*, **94**, 5369, 1990.
- Clegg, S. L., and P. Brimblecombe, A generalized multicomponent thermodynamic model applied to the $(\text{NH}_4)_2\text{SO}_4-\text{H}_2\text{SO}_4-\text{H}_2\text{O}$ system to high supersaturation and low relative humidity at 298.15K, *J. Aerosol Sci.*, **26**, 19, 1995a.
- Clegg, S. L., and P. Brimblecombe, Application of a multicomponent thermodynamic model to activities and thermal properties of 0–40 mol kg^{-1} aqueous sulfuric acid from < 200 to 328K, *J. Chem. Eng. Data*, **40**, 43, 1995b.
- Clegg, S. L., P. Brimblecombe, and A. S. Wexler, A thermodynamic model of the system $\text{H}^+-\text{NH}_4^+-\text{O}_4^{2-}-\text{NO}_3^- - \text{H}_2\text{O}$ at tropospheric temperatures, *J. Phys. Chem. A*, **102**, 2137, 1998a.
- Clegg, S. L., P. Brimblecombe, and A. S. Wexler, A thermodynamic model of the system $\text{H}^+-\text{NH}_4^+-\text{Na}^+-\text{SO}_4^{2-}-\text{NO}_3^- - \text{Cl}^- - \text{H}_2\text{O}$ at 298.15K, *J. Phys. Chem. A*, **102**, 2155, 1998b.
- Jacobson, M. Z., *Fundamentals of Atmospheric Modeling*, Cambridge Univ. Press, New York, 1999a.
- Jacobson, M. Z., Studying the effects of calcium and magnesium on size-distributed nitrate and ammonium with EQUISOLV II, *Atmos. Environ.*, **33**, 3635, 1999b.
- Jacobson, M. Z., A physically-based treatment of elemental carbon optics: Implications for global direct forcing of aerosols, *Geophys. Res. Lett.*, **27**, 217, 2000.
- Jacobson, M. Z., A. Tabazadeh, and R. P. Turco, Simulating equilibrium within aerosols and nonequilibrium between gases and aerosols, *J. Geophys. Res.*, **101**, 9079, 1996.
- Kärcher, B., and S. Solomon, On the composition and optical extinction of particles in the tropopause region, *J. Geophys. Res.*, **104**, 27,441, 1999.
- Kim, Y. P., and J. H. Seinfeld, Atmospheric gas-aerosol equilibrium, III, Thermodynamics of crustal elements Ca^{2+} , K^+ , and Mg^{2+} , *Aerosol Sci. Technol.*, **22**, 93, 1995.
- Kusik, C. L., and H. P. Meissner, Electrolyte activity coefficients in inorganic processing, *AIChE Symp. Ser.*, **74**, 14, 1978.
- Laaksonen, A., J. Hienola, and M. Kulmala, Supercooled cirrus cloud formation modified by nitric acid pollution of the upper troposphere, *Geophys. Res. Lett.*, **24**, 3009, 1997.
- Luo, B., K. S. Carslaw, T. Peter, and S. L. Clegg, Vapor pressures of $\text{H}_2\text{SO}_4/\text{HNO}_3/\text{HCl}/\text{HBr}/\text{H}_2\text{O}$ solutions to low stratospheric temperatures, *Geophys. Res. Lett.*, **22**, 247, 1995.
- Pilius, C., and J. H. Seinfeld, Continued development of a general equilibrium model for inorganic multicomponent atmospheric aerosols, *Atmos. Environ.*, **32**, 2453, 1987.
- Pitzer, K. S., *Activity Coefficients in Electrolyte Solutions*, 2nd ed., CRC Press, Boca Raton, Fla., 1991.
- Saxena, P., C. Seigneur, A. B. Hudischewskyj, and J. H. Seinfeld, A comparative study of equilibrium approaches to the chemical characterizations of secondary aerosols, *Atmos. Environ.*, **20**, 1471, 1986.
- Solomon, S., Stratospheric ozone depletion: A review of concepts and history, *Rev. Geophys.*, **37**, 275, 1999.
- Stelson, A. W., and J. H. Seinfeld, Relative humidity and temperature dependence of the ammonium nitrate dissociation constant, *Atmos. Environ.*, **26**, 983, 1981.
- Stokes, R. H., and R. A. Robinson, Interactions in aqueous nonelectrolyte solutions, I. solute-solvent equilibria, *J. Phys. Chem.*, **70**, 2126, 1966.

- Tabazadeh, A., and O. B. Toon, The role of ammoniated aerosols in cirrus cloud nucleation. *Geophys. Res. Lett.*, **25**, 1379, 1998.
- Tabazadeh, A., R. P. Turco, and M. Z. Jacobson, A model for studying the composition and chemical effects of stratospheric aerosols, *J. Geophys. Res.*, **99**, 12,897, 1994.
- Tabazadeh, A., O. B. Toon, S. Clegg, and P. Hamill, A new parameterization of $\text{H}_2\text{SO}_4/\text{H}_2\text{O}$ aerosol composition: Atmospheric implications, *Geophys. Res. Lett.*, **24**, 1931, 1997a.
- Tabazadeh, A., O. B. Toon, and E. Jensen, Formation and implications of ice particle nucleation in the stratosphere, *Geophys. Res. Lett.*, **24**, 2007, 1997b.
- Tabazadeh, A., M. Z. Jacobson, H. B. Singh, O. B. Toon, J. S. Lin, B. Chatfield, A. N. Thakur, R. W. Talbot, and J. E. Dibb, Nitric acid scavenging by mineral and biomass aerosols, *Geophys. Res. Lett.*, **25**, 4185, 1998.
- Talbot, R. W. et al., Chemical characteristics of continental outflow from Asia to the troposphere over the western Pacific Ocean during September-October 1991: Results from PEM-West A, *J. Geophys. Res.*, **101**, 1713, 1996.
- Talbot, R. W., J. E. Dibb, and M. B. Loomis, Influence of vertical transport on free tropospheric aerosols over the central USA in springtime, *Geophys. Res. Lett.*, **25**, 1367, 1998.
- Weisenstein, D. K., Y. K. Glenn, M. K. W. Ko, N. Sze, J. M. Rodriguez, and C. J. Scott, A two-dimensional model of sulfur species and aerosols, *J. Geophys. Res.*, **102**, 13,019, 1997.
- Wexler, A. S., and J. H. Seinfeld, Second-generation inorganic aerosol model, *Atmos. Environ., Part A*, **25**, 2731, 1991.
- Xu, J., D. Imre, R. McGraw, and I. Tang, Ammonium sulfate: Equilibrium and metastability phase diagrams from 40°C to -50°C, *J. Phys. Chem. B*, **102**, 7462, 1998.
- J. S. Lin and A. Tabazadeh, NASA Ames Research Center, MS 245-4, Moffett Field, CA 94035. (lin@ice.arc.nasa.gov; atabazadeh@mail.arc.nasa.gov)

(Received May 11, 2000; revised August 29, 2000; accepted September 15, 2000.)

Submitted to *J. Geophys. Res.*, October 2000

The onset, extent and duration of dehydration in the Southern Hemisphere polar vortex

Elizabeth M. Stone, Azadeh Tabazadeh and Eric Jensen

NASA Ames Research Center, Moffett Field, California

Hugh C. Pumphrey

Department of Meteorology, University of Edinburgh, UK

Michelle L. Santee

Jet Propulsion Laboratory, California Institute of Technology, Pasadena, California

John L. Mergenthaler

Lockheed Martin Advanced Technology Center, Palo Alto, California

Abstract.

Satellite observations of water vapor and aerosol extinction along with temperature trajectory calculations are analyzed for the Southern Hemisphere winter of 1992 in order to determine the onset, extent and duration of dehydration within the polar vortex. Our investigation utilizes measurements of water vapor from the Microwave Limb Sounder (MLS) and extinction from the Cryogenic Limb Array Etalon Spectrometer (CLAES) both onboard the Upper Atmosphere Research Satellite (UARS). Evidence for dehydration is seen on potential temperature surfaces from 420-520 K (approximately 16 to 22 km). The horizontal extent of the dehydrated area at 465 K encompasses up to 35% of the total vortex area. Based on MLS observations and temperature statistics, the onset of dehydration occurs between late June and early July, and dehydrated regions persist well into November. A comparison of CLAES aerosol extinction measurements and model calculations of extinction suggests an average ice particle number concentration and size of 10^{-2} - 10^{-3} cm $^{-3}$ and 10-30 μ m, respectively. We show that the difference in timing of the onset of dehydration found here and in a recent analysis of Polar Ozone and Aerosol Measurement III (POAM) observations is due to the latitudinal sampling pattern of the POAM instrument.

1. Introduction

Polar stratospheric clouds (PSCs) form in the low temperatures of the winter polar vortex and have a direct influence on atmospheric chemistry by their involvement in heterogeneous ozone chemistry [Solomon, 1999]. PSCs also act as a sink for gas phase water vapor and nitric acid resulting in stratospheric dehydration [e.g., Kelly *et al.*, 1989; Hofmann

and Deshler, 1991; Nedoluha *et al.*, 2000] and denitrification [e.g., Toon *et al.*, 1986; Santee *et al.*, 1999; Tabazadeh *et al.*, 2000a].

Understanding the physical properties of the clouds and the meteorological conditions under which they form is important for studies of the polar vortex. Particle size and composition influence the optical properties of the clouds, which affect remote sensing [Toon *et al.*, 1990; Browell *et al.*,

1990]; composition of the aerosols impacts constituent budgets and chemical reactions [Solomon, 1999]; and chemical processes which are dependent upon relative humidity will be affected by the deficit of water vapor due to dehydration [Hanson et al., 1994]. PSCs are separated into two types [WMO, 1999]. Type II PSCs are composed of water ice and form at temperatures below the ice frost point. Type I clouds form at temperatures above the ice frost point and consist of both liquid and solid nitric acid-containing cloud particles. We focus our study on the atmospheric dehydration process which occurs as a result of ice particle growth and sedimentation, thereby removing water from the atmosphere.

The Airborne Antarctic Ozone Experiment (AAOE) in August–September 1987 showed the first evidence of stratospheric dehydration in the Antarctic vortex [Kelly et al., 1989]. Balloon measurements in the Antarctic have also shown profiles with water vapor depletion [Hofmann et al., 1991; Rosen et al., 1988; Vömel et al., 1995]. Using balloon measurements over McMurdo in 1994, Vömel et al. [1995] conclude that dehydration starts around mid June and persists into November. Overall, only a limited number of *in situ* measurements have been made over the Antarctic region over the course of several winters. Satellite observations can provide a more extensive view of the polar regions. Springtime dehydration has been noted in the analysis of Halogen Occultation Experiment (HALOE) data [Pierce et al., 1994; Rosenlof et al., 1997]. Santee et al. [1995] report on the interhemispheric differences in wintertime water vapor from the Microwave Limb Sounder (MLS) and Ricaud et al. [1995] deduce PSCs from MLS water vapor and Cryogenic Limb Array Etalon Spectrometer (CLAES) extinction measurements from several days in August–September 1992. Evidence for wintertime dehydration is also found in measurements from the Atmospheric Trace Molecule Spectroscopy (ATMOS) instrument [Manney et al., 1999], and Nedoluha et al. [2000] report on Polar Ozone and Aerosol Measurement III (POAM) observations which show dehydration occurring in the Southern Hemisphere (SH) winter of 1998.

In our study, we examine satellite measurements of stratospheric water vapor and extinction in the SH winter polar regions to identify the onset, extent and duration of dehydration. We correlate water vapor concentrations with aerosol extinction and use temperature trajectories to examine where and when the dehydration process occurs. We compare measured and calculated extinction to infer ice particle size and number density in the dehydration column.

2. Observations

Water vapor data for this study come from the MLS instrument onboard the Upper Atmosphere Research Satellite (UARS). We use the prototype water vapor product (version 104) described by Pumphrey [1999], which gives water vapor mixing ratios in the stratosphere from 0.1 to 100 hPa with a vertical resolution of 3–4 km. Although this product is not an official UARS project MLS product, its validity and usefulness in scientific studies has been demonstrated [Pumphrey et al., 2000; Pumphrey, 1999; Manney et al., 1998]. The water vapor measurements are available from September 1991 to April 1993, which includes only one SH winter.

The CLAES instrument, also onboard UARS, measures aerosol extinction coefficients [Mergenthaler et al., 1997] which have been used to identify PSCs [Mergenthaler et al., 1997; Ricaud et al., 1995; Massie et al., 1994] and to determine volume and surface area densities of type I PSCs [Massie et al., 1997, 1998]. In identifying PSCs, extinction values are generally used qualitatively and threshold values for PSCs, depending on pressure, are determined relative to temperature and pre-winter observations. No information on particle size and concentration is given with the aerosol extinction data product. CLAES was operational from September 1991 until May 1993. Our analysis uses the CLAES version 8 extinction coefficients at 780 cm^{-1} .

MLS and CLAES measurements are nearly coincident in time and space, each with a horizontal resolution of $\sim 400\text{ km}$. The vertical profiles of water vapor and extinction have been interpolated from the standard UARS grid to potential temperature surfaces using United Kingdom Meteorological Office (UKMO) temperatures. UKMO temperatures are also used for the analysis in sections 2 and 3. Comparisons of the UKMO temperatures with radiosonde observations show that systematic biases are less than 1 K throughout the SH winter [Manney et al., 1996].

We focus on the UARS SH viewing periods for one year, starting in April 1992 (1–30 April 1992, 2 June–12 July 1992, 14 August–20 September 1992, 30 October–28 November 1992, 10 January–8 February 1993, and 20 March–1 April 1993). We note that there are significant data gaps in the June–July viewing period due to problems with the UARS solar array which required the MLS and CLAES instruments to be turned off. Data availability limits this study to only one SH winter and we therefore do not assess year-to-year variability of dehydration. Although the SH winter of 1992 was not necessarily a typical year since there were high levels of stratospheric aerosol from Pinatubo, the duration of cold temperatures and minimum temperatures were typical of wintertime conditions.

The water vapor annual cycles on potential temperature surfaces, compiled from the high-latitude MLS data, are shown in Figure 1. Daily averages are from data in the 70°S–80°S latitude range for one year starting in April 1992. The 420 K potential temperature level is below 100 hPa in January through March, resulting in a lack of observations on that surface during that time. Potential temperature surfaces from 420 to 585 K show a minimum in water vapor in the winter months. These potential temperature surfaces cover pressure levels of 100 to 15 hPa. Since the water vapor data set does not extend below 100 hPa, we cannot observe the lower altitude limit of the dehydration. Nedoluha *et al.* [2000] show evidence for dehydration down to 12 km. At the higher potential temperature surfaces, the maximum in the annual cycle is found in late winter (August–September). The depleted winter values at and below 585 K are a result of cold temperatures found within the polar vortex. Average temperatures in July on the 465 K potential temperature surface are near 185 K, below the ice frost point (188 K). Ice clouds form at these cold temperatures and deplete the gas phase water.

The daily averages of aerosol extinction from CLAES are also shown in Figure 1. In general, they are anti-correlated with the water vapor in the winter months from 420 to 585 K. High extinction values are seen from mid June through late August when the water vapor mixing ratios are low, reinforcing the observation that the deficit in gas phase water coincides with the presence of PSCs. Extinction values in September are lower than the pre-winter values. This feature in the annual development of extinction has been seen by other observations and is due to the cleansing of the atmosphere by the subsidence of PSCs and by descent in the vortex [Kent *et al.*, 1985; Thomason and Poole, 1993; Randall *et al.*, 1996; Nedoluha *et al.*, 2000].

Due to limited MLS water vapor measurements in late June and early July, we cannot observe the precise onset of dehydration. The measurements indicate that dehydration begins sometime after June 18. Extinction values are already high prior to June 18 due to Type I PSCs [Tabazadeh *et al.*, 2000a], which form at temperatures higher than the ice frost point. A deficit in the water vapor mixing ratio is clearly seen in the July 10–12 measurements for the 420 to 585 K surfaces. At 465 K, daily average values have dropped from 4 ppmv in mid June to 2.7 ppmv on July 10, indicating that the onset of substantial dehydration occurred sometime after mid June and before 10 July. Water vapor values at the 420 K and 465 K levels drop further between mid July and early August when the next observation period begins. In August–September, daily mean values are between 2.3 and 2.8 ppmv at 465 K. Extinction values are still elevated in mid August but have diminished by early September. Measure-

ments on the 585 K surface show a drop in the water vapor and an elevation of extinction in mid July, but values have recovered by August, indicating that the initial drop in water vapor seen at this level was reversible or that mixing ratios are replenished by the descent of moister air from above.

Figure 1 depicts only daily averages in the 70°S–80°S latitude range. Additional information can be found in the distributions of water vapor and extinction measurements. Figures 2a and 2b show distributions of water vapor and aerosol extinction in the region of 50°S–80°S for different temperature bins ($T < 185$ K, $185 < T < 188$ K, $188 < T < 195$ K, and $195 < T < 210$ K (points with temperatures greater than 210 K are excluded)). We also show the distributions of water vapor and extinction for the 70°S–80°S latitude bin (for all temperatures). The $T < 185$ K bin represents air below the ice nucleation point (typically 3–4 K below the frost point [Tabazadeh *et al.*, 2000b; Chang *et al.*, 1999]) and the $185 < T < 188$ K bin represents observations between the frost point and the nucleation point. The distributions for data taken between April and November 1992 are separated according to the UARS yaw cycle.

We use the high latitude April measurements, representing pre-wintertime observations, to define low water vapor and high extinction values later in the paper. The water vapor distribution peaks at 4.3 ppmv in April and all the extinction values in this month are less than 0.0009 km^{-1} . In June–July, the mode of the water vapor distribution for $T < 185$ K is 2.3 ppmv and the $185 < T < 188$ K observations have two peaks at 2.3 ppmv and near 4 ppmv. For $T > 188$ K the distributions are centered at 4 ppmv and fewer than 10% of the observations are less than 3.5 ppmv, indicating that by this time the dehydrated area has not yet spread beyond the stability region of ice particles. Therefore, we define dehydrated areas to have water vapor mixing ratios less than 3.0 ppmv based on the April measurements, and “high” aerosol extinction is defined to be values larger than 0.001 km^{-1} . The aerosol extinction threshold is slightly higher than the value used to identify PSCs at 46 hPa (0.00075 km^{-1}) by Mergenthaler *et al.* [1997]. Extinction values over 0.002 km^{-1} have large uncertainties due to the high optical depth of the PSCs along the limb viewing path [Mergenthaler *et al.*, 1997]. However, the uncertainties do not affect the classification of “high” aerosol amount. The June–July distributions show that nearly all the observations which coincide with temperatures below 185 K are dehydrated. 25% of the observations with $185 < T < 188$ K are dehydrated. For temperatures above 188 K, there is no evidence of significant depletion of the water vapor.

The extinction distributions for the June–July observation period show evidence of both Type I and Type II PSCs. The temperature bins with $T < 195$ K all show observa-

tions of extinction above the April distributions. For the $185 < T < 188$ K temperature bin, 75% of the observations have extinctions larger than the pre-winter values. This is significantly larger than the 25% of water vapor measurements that show a deficit in this temperature bin, suggesting that type I PSCs are contributing to the elevated extinction. The coldest temperatures coincide with the highest extinction values. All of the observations with $T > 195$ K show low extinction values, less than 0.001 km^{-1} .

By the August–September viewing period, the distributions of water vapor mixing ratios for all temperature bins with $T < 195$ K peak near 2.2 ppmv. For $195 < T < 210$ K, the majority of the observations are centered around 4 ppmv but there are measurements with mixing ratios less than 3 ppmv in this temperature range as well. The extinction distributions during this time have a small percentage of observations with extinctions above 0.001 km^{-1} and these coincide with the coldest temperatures ($T < 188$ K). Thus by this time in the winter, there exist dehydrated mixing ratios that do not directly coincide with low temperatures or high extinction values.

Although temperatures at high latitudes are warmer by November, water vapor mixing ratios have recovered only slightly from the dehydration. The distribution for 70°S – 80°S peaks at 3.0 ppmv. While some water vapor recovery has taken place in November, the overall mixing ratios are still substantially below the April mode value (~ 4.3 ppmv) before any dehydration occurred.

3. Extent and Timing of Dehydration

In this section we quantify the horizontal extent of the dehydration, its development throughout the winter months, and its relationship to the areas of cold temperatures, high extinction, and the vortex. To do this, we calculate the area encompassing the vortex and the regions of dehydrated air, high extinction, and cold temperatures. Criteria for dehydration (mixing ratios less than 3.0 ppmv) and “high” extinction (larger than 0.001 km^{-1}) are determined from the frequency distributions in the early winter months and before the onset of winter (Figures 2a and 2b). The water vapor distributions for early winter show two peaks, separated near 3 ppmv, and April measurements all exceed 3 ppmv (Figure 2a). The extinction distributions in early winter show a distinct separation at 0.001 km^{-1} and pre-winter values are all below that threshold (Figure 2b). The cold temperature criteria are the frost point of ice ($T < 188$ K) and the ice nucleation temperature (typically 3 K less than the frost point, $T < 185$ K [Tabazadeh *et al.*, 2000b; Chang *et al.*, 1999]). We use a scaled potential vorticity value of 1.4 s^{-1} to approximate the vortex boundary. Figure 3 shows the calculated daily areas

from April through November on the 465 K potential temperature surface.

The area of temperatures below the frost point of ice begins to develop in mid June. At this time high extinction values are present but there is no evidence of dehydration. The area of high extinction values drops on June 24 and then increases again. Tabazadeh *et al.* [2000a] show that denitrification at 450 K occurred over 12 days from June 12–24. Temperatures below the ice nucleation point are present over a small area in mid June but do not persist or develop over larger areas until after June 27. By July 10, the area of dehydration coincides roughly with the area of temperatures below the ice nucleation point and is similar to the area of high extinction. When water vapor measurements are available again in mid August, the dehydrated area exceeds the cold temperature area and persists at $12 \times 10^6 \text{ km}^2$ through most of September, consistent with observations by [Vömel *et al.*, 1995] in which they find that the water vapor profiles from early August and early October in 1994 at McMurdo Station are similar. From mid August through late September the dehydrated area is roughly 30%–35% of the total vortex area. Cold temperature areas decrease rapidly at the end of August. The area of high extinction is much less than the dehydrated area during August and September, indicating that the dehydration persists after the ice clouds have precipitated. The dehydrated areas persist and remain at nearly a constant value (from early August to late September) after the area of high extinction (indicating the presence of clouds) has vanished in early September and after the vortex area begins to recede in early September. The dehydrated area decreases rapidly after November 15, and the water vapor values start a rapid recovery. The water vapor mixing ratios at 465 K (Figure 1) show an increase between mid September and the beginning of November similar to what is observed for nitric acid [Santee *et al.*, 1999]. The dehydrated area in Figure 3 does not show this recovery occurring since the area will not start to decrease until mixing ratios surpass 3 ppmv, indicating that mixing ratios are attaining values similar to those present before temperatures fell below the ice frost point.

4. Temperature Statistics

The interpretation of the time development of the area of dehydration compared to the area of cold temperatures (Figure 3) is limited in that it does not include the temperature history of air parcels. Tabazadeh *et al.* [2000a] utilize the concept of “PSC lifetimes” to examine how long an air mass persists at temperatures less than the condensation points of nitric acid trihydrate (NAT), nitric acid dihydrate (NAD), and water ice. In this section, we use temperature statistics from National Centers for Environmental Predic-

tion (NCEP) trajectory calculations to look at the onset of temperatures which meet the ice nucleation conditions for the formation and growth of water ice clouds.

For each day in June through September, 20 points were homogeneously distributed within the 188 K temperature contour at 50 hPa. Twenty forward and backward trajectories were run isentropically from the initialized points for 14 days. Diabatic descent, which can impact the Antarctic lower stratosphere over a 14-day period in midwinter, is neglected in these calculations. The statistics of the trajectory analysis are shown in Figure 4. The solid line depicts the percentage of trajectories for each day that have passed through the ice nucleation criterion (reaching temperatures of about 185 K or below). Symbols show the average, minimum and maximum time that the ensemble of trajectories spends below the ice frost point (188 K) after the nucleation criterion has been met. The temperature statistics suggest that the onset of dehydration occurred at the end of June when a significant number of the trajectories met the nucleation criterion for the formation of ice particles. By early July, 60 to 90% of the parcels encountered temperatures below 185 K, suggesting that by this time ice particles nucleated in nearly all the air parcels initialized within the 188 K temperature contour. In addition, the lifetime of ice particles nucleated was long enough (5 days or longer) to provide sufficient time for growth and sedimentation of particles to lower altitudes.

5. Model Extinctions

Next we focus on the extinction measurements from CLAES. Previous studies have used these measurements to identify PSCs [Mergenthaler *et al.*, 1997; Ricaud *et al.*, 1995; Massie *et al.*, 1994]. Here we use Mie calculations to compute aerosol extinction due to ice particles. The calculated extinction values are compared to the CLAES observations to infer ice particle size and number density.

Our calculated extinction depend upon temperatures, pressure, water vapor mixing ratio and fraction of aerosols nucleated into ice particles. To compute the extinction, we have distributed the volume of condensed water (as ice) at equilibrium over a fixed and assumed number density of ice particles. The size of the ice particles obtained in this manner, for a given number density, were used as input parameters into a Mie code to convert the volume and size information into extinction units [Toon *et al.*, 1990; Massie *et al.*, 1994]. The CLAES observations are compared with extinction calculated using different assumptions as to the number density of ice particles based on the range of number densities observed in the in situ data [Hofmann *et al.*, 1991]. Maps of the calculated extinction are formed by computing the extinc-

tion for the temperatures at the geographic locations of the CLAES measurements when the temperature is below the threshold for type II PSCs (188 K). At locations where this temperature criterion is not met, the observed CLAES values are used in constructing the extinction maps. The maps depict what the CLAES instrument would have observed if type II PSCs were present in the locations where they are predicted to form and if the instrument measured perfectly. We examine days from early in the winter since once condensation and ice particle formation begins, the amount of water vapor available changes. For the early wintertime conditions, we use a mixing ratio of 4.1 ppmv, based on the mean values in Figure 1. Figure 5 shows maps of the CLAES data and calculated extinction for three different assumptions of ice particle density. The figure shows that an ice particle number density in the range of 10^{-2} – 10^{-3} cm^{-3} best matches the CLAES observations. The comparison between the observed and calculated extinction is good despite the uncertainty in the CLAES measurements for high values of extinction. Based on the modeling analyses of Jensen and Toon [1994], the low ice number density implies that the clouds were formed in regions with very slow cooling.

The size of ice particles associated with the concentrations of 10^{-2} – 10^{-3} cm^{-3} is shown in Figure 6. The distributions are formed from the calculated sizes for the days in Figure 5. Ice particle sizes are on the order of 10–30 μm . These should be considered general values since the real atmosphere is likely to contain a distribution of ice particle number densities and sizes. In general our inferred ice particle number density and size are in good agreement with balloon observations over McMurdo station [Hofmann *et al.*, 1991].

6. Comparison of dehydration from POAM and MLS

A recent study of water vapor and extinction data from POAM III examines dehydration in the Antarctic for the SH winter of 1998 [Nedoluha *et al.*, 2000]. POAM is a solar occultation instrument and makes 14 measurements per day in each hemisphere around a latitude circle. The latitude sampled varies semi-annually as shown in Figure 7. The POAM instrument measures water vapor and extinction with a high vertical resolution (~ 1 km) in the lower stratosphere, making it useful for studies of dehydration and PSC occurrence. Nedoluha *et al.* [2000] report dehydration occurring over a 6 week period starting in mid July with the drop in water vapor coincident with the timing of the minimum temperatures dropping below the ice frost point in air parcels sampled by the POAM instrument and with the occurrence of a significant number of extinction measurements indicating

the presence of type II PSCs.

While the data used in our study cover a different calendar year, we note that our analysis of the water vapor mixing ratios from MLS and temperature statistics suggests that the onset of dehydration begins prior to early July, and it is therefore necessary that we relate our conclusions to those of Nedoluha *et al.* [2000]. MLS mixing ratios from 70°S to 80°S drop significantly (from 4 to 2.7 ppmv) from mid June to July 10 (Figure 1). The area of dehydration and cold temperatures begins to develop in late June (Figure 3). Vömel *et al.* [1995] suggest that dehydration and the cold temperature regions develop initially in the interior of the vortex and expand outward. Thus the first observation of dehydrated air depends upon the latitude being sampled. From late June through mid July, the POAM instrument observes latitudes from 65°S–70°S. The MLS water vapor measurements in this latitude range do not show evidence of significant dehydration in 10–12 July (Figure 7), whereas substantial dehydration is evident in the MLS data closer to the pole (70°S–80°S) for those dates. Because MLS shows no signs of dehydration in mid June and substantial dehydration on 10 July, we conclude that the onset of severe dehydration occurred sometime between mid June and 10 July. Further, temperature statistics provide additional support for the onset of dehydration to be around late June. Therefore, if the meteorological conditions during the 1992 and 1998 Antarctic southern winters are comparable, then the onset of dehydration observed by POAM type instruments will always be offset as compared to the onset seen by MLS type instruments. By August, POAM is observing latitudes poleward of 70°S and deficits in the water vapor are apparent in the data during this period [Nedoluha *et al.*, 2000]. Thus, while the analysis of the POAM data provides a much finer vertical picture and more continuous daily measurements than does the MLS data, it is important to note that the latitudinal sampling influences the determination of the onset of dehydration.

7. Summary

Examining satellite measurements of water vapor from the SH winter of 1992, we find evidence for dehydration due to the formation of type II PSCs on potential temperature surfaces from 420 to 520 K (16 to 22 km). However, POAM observations of water vapor show that dehydration extends down to ~360 K (12 km). Thus the vertical extent of dehydration is at least 4 km deeper than what MLS can see, according to the POAM data. The deficits in water vapor are seen in measurements from mid July persisting into November. Mean mixing ratios decrease by approximately 1 to 2 ppmv. Temperature statistics suggest that the onset of dehy-

dration occurs in late June when a large number of cold air mass trajectories meet the ice nucleation criteria. Because the onset of dehydration initially occurs close to the pole, the latitudinal sampling of the atmosphere by different instruments must be taken into account for the determination of the dehydration onset. The development of dehydration over the course of the winter shows that initially (June–July observations) dehydration is found only in areas which have cold temperatures (below 188 K). These areas coincide with those with high aerosol extinction. Area calculations show that regions which meet the cold temperature criteria and those which meet the criteria for dehydrated air expand throughout July. By August, the dehydrated regions are larger than those of the cold temperatures and high extinction. The dehydrated mixing ratios persist after the elevated extinction and cold temperatures diminish. Results from a Mie code calculation in conjunction with the extinction measurements give a general estimate of aerosol properties. A number density between 10^{-2} – 10^{-3} cm⁻³ best matches the observed extinction and, our estimate of ice particle size is on the order of 10–30 μ m.

Acknowledgments. This work is supported by the NASA Upper Atmosphere Research Satellite Program. Temperature histories used here were obtained from the Goddard Space Flight Center automailer system.

References

- Browell, E. V., C. F. Butler, S. Ismail, P. A. Robinette, A. F. Carter, N. S. Higdon, O. B. Toon, M. R. Schoeberl, and A. F. Tuck, Airborne lidar observations in the wintertime Arctic stratosphere: Polar stratospheric clouds, *Geophys. Res. Lett.*, **17**, 385–388, 1990.
- Chang, H. A., T. Koop, L. T. Molina, and M. J. Molina, Phase transition in emulsified HNO₃/H₂O and HNO₃/H₂SO₄/H₂O solutions, *J. Phys. Chem.*, **103**, 2673–2679, 1999.
- Hanson, D. H., A. R. Ravishankara, and S. Solomon, Heterogeneous reactions in sulfuric acid aerosols: A framework for model calculations, *J. Geophys. Res.*, **99**, 3615–3629, 1994.
- Hofmann, D. J., and T. Deshler, Stratospheric cloud observations during formation of the Antarctic ozone hole in 1989, *J. Geophys. Res.*, **96**, 2897–2912, 1991.
- Hofmann, D. J., S. J. Oltmans, and T. Deshler, Simultaneous balloon-borne measurements of stratospheric water vapor and ozone in the polar regions, *Geophys. Res. Lett.*, **18**, 1011–1014, 1991.
- Jensen, E., and O. B. Toon, Ice nucleation in upper troposphere: Sensitivity to aerosol number density, temperature, and cooling rate, *Geophys. Res. Lett.*, **21**, 2019–2022, 1994.
- Kelly, K. K., et al., Dehydration in the lower Antarctic stratosphere during late winter and early spring, *J. Geophys. Res.*, **94**, 11317–11357, 1989.
- Kent, G. S., C. R. Trepte, U. O. Farrukh, and M. P. McCormick, Variation in the stratospheric aerosol associated with the north

- cyclonic polar vortex as measured by the SAM II satellite sensor, *J. Atmos. Sci.*, **42**, 1536–1551, 1985.
- Manney, G. L., R. Swinbank, S. T. Massie, M. E. Gelman, A. J. Miller, R. Nagatani, A. O'Neill, and R. W. Zurek, Comparison of U. K. Meteorological Office and U. S. National Meteorological Center stratospheric analyses during northern and southern winter, *J. Geophys. Res.*, **101**, 10311–10334, 1996.
- Manney, G. L., Y. J. Orsolini, H. C. Pumphrey, and A. E. Roche, The 4-day wave and transport of UARS tracers in the austral polar vortex, *J. Atmos. Sci.*, **55**, 3456–3470, 1998.
- Manney, G. L., H. A. Michelsen, M. L. Santee, M. R. Gunson, F. W. Irion, A. E. Roche, and N. J. Livesey, Polar vortex dynamics during spring and fall diagnosed using trace gas observations from the Atmospheric Trace Molecule Spectroscopy instrument, *J. Geophys. Res.*, **104**, 18841–18866, 1999.
- Massie, S. T., D. Baumgardner, and J. E. Dye, Estimation of polar stratospheric cloud volume and area densities from UARS, stratospheric aerosol measurement II, and polar ozone and aerosol measurement II extinction data, *J. Geophys. Res.*, **103**, 5773–5783, 1998.
- Massie, S. T., et al., Spectral signatures of polar stratospheric clouds and sulfate aerosol, *J. Atmos. Sci.*, **51**, 3027–3044, 1994.
- Massie, S. T., et al., Simultaneous observations of Polar Stratospheric Clouds and HNO₃ over Scandinavia in January, 1992, *Geophys. Res. Lett.*, **24**, 595–598, 1997.
- Mergenthaler, J. L., J. B. Kumer, A. E. Roche, and S. T. Massie, Distribution of antarctic polar stratospheric clouds as seen by the CLAES experiment, *J. Geophys. Res.*, **102**, 19161–19170, 1997.
- Nedoluha, G. E., R. M. Bevilacqua, K. W. Hoppel, M. Daehler, E. P. Shettle, J. H. Hornstein, M. D. Fromm, J. D. Lumpe, and J. E. Rosenfield, POAM III measurements of dehydration in the Antarctic lower stratosphere, *Geophys. Res. Lett.*, **27**, 1683–1686, 2000.
- Pierce, R. B., W. L. Grose, J. M. Russell III, A. F. Tuck, R. Swinbank, and A. O'Neill, Spring dehydration in the Antarctic stratospheric vortex observed by HALOE, *J. Atmos. Sci.*, **51**, 2931–2941, 1994.
- Pumphrey, H. C., Validation of a prototype water vapor retrieval for UARS MLS, *J. Geophys. Res.*, **104**, 9399–9412, 1999.
- Pumphrey, H. C., H. L. Clark, and R. S. Harwood, Lower stratospheric water vapor measured by UARS MLS, *Geophys. Res. Lett.*, **27**, 1691–1694, 2000.
- Randall, C. E., et al., An overview of POAM II aerosol measurements at 1.06 μm , *Geophys. Res. Lett.*, **23**, 3195–3198, 1996.
- Ricaud, P. D., et al., Polar stratospheric clouds as deduced from MLS and CLAES measurements, *Geophys. Res. Lett.*, **22**, 2033–2036, 1995.
- Rosen, J. M., D. J. Hofmann, J. R. Carpenter, J. W. Harder, and S. J. Oltmans, Balloon-borne Antarctic frost point measurements and their impact on polar stratospheric cloud theories, *Geophys. Res. Lett.*, **15**, 859–862, 1988.
- Rosenlof, K. H., A. F. Tuck, K. K. Kelly, J. M. Russell III, and M. P. McCormick, Hemispheric asymmetries in water vapor and inferences about transport in the lower stratosphere, *J. Geophys. Res.*, **102**, 13,213–13,234, 1997.
- Santee, M. L., W. G. Read, J. W. Waters, L. Froidevaux, G. L. Manney, D. A. Flower, R. F. Jarnot, R. S. Harwood, and G. E. Peckham, Interhemispheric differences in polar stratospheric HNO₃, H₂O, ClO and O₃, *Science*, **267**, 849–852, 1995.
- Santee, M. L., G. L. Manney, L. Froidevaux, W. G. Read, and J. W. Waters, Six years of UARS Microwave Limb Sounder HNO₃ observations: Seasonal, interhemispheric, and interannual variations in the lower stratosphere, *J. Geophys. Res.*, **104**, 8225–8246, 1999.
- Solomon, S., Stratospheric ozone depletion: A review of concepts and history, *Rev. Geophys.*, **37**, 275–316, 1999.
- Tabazadeh, A., M. L. Santee, M. Y. Danilin, H. C. Pumphrey, P. A. Newman, P. J. Hamill, and J. L. Mergenthaler, Quantifying denitrification and its effect on ozone recovery, *Science*, **288**, 1407–1411, 2000a.
- Tabazadeh, A., S. T. Martin, and J. S. Lin, The effect of particle size and nitric acid uptake on the homogeneous freezing of aqueous sulfuric acid particles, *Geophys. Res. Lett.*, **27**, 1111–1114, 2000b.
- Thomason, L. W., and L. R. Poole, Use of stratospheric aerosol properties as diagnostics of Antarctic vortex processes, *J. Geophys. Res.*, **98**, 23003–23012, 1993.
- Toon, O. B., P. Hamill, R. P. Turco, and J. Pinto, Condensation of HCl and HNO₃ in the winter polar stratosphere, *Geophys. Res. Lett.*, **13**, 1284–1287, 1986.
- Toon, O. B., E. V. Browell, S. Kinne, and J. Jordan, An analysis of lidar observations of polar stratospheric clouds, *Geophys. Res. Lett.*, **17**, 393–396, 1990.
- Vömel, H., S. J. Oltmans, D. J. Hofmann, T. Deshler, and J. M. Rosen, The evolution of the dehydration in the Antarctic stratospheric vortex, *J. Geophys. Res.*, **100**, 13919–13926, 1995.
- WMO, Scientific assessment of ozone depletion: 1998, Rep. 44, 1999.
- H. C. Pumphrey, Department of Meteorology, The University of Edinburgh, Edinburgh UK EH9 3JZ
- Michelle Santee, Jet Propulsion Laboratory, 4800 Oak Grove Drive, MS 183-701, Pasadena, CA 91109-8099.
- Eric Jensen and Elizabeth M. Stone and Azadeh Tabazadeh, Mail Stop 245-4, NASA Ames Research Center, Moffett Field, CA
- John L. Mergenthaler, Lockheed Martin Advanced Technology Center, 3251 Hanover Street, Palo Alto, California 94304

??-??-00; revised ??-??-00; accepted ??-??-00.